Applied Geochemistry 87 (2017) 1–21

Contents lists available at ScienceDirect

Applied Geochemistry

journal homepage: www.elsevier.com/locate/apgeochem

Hydrogeochemical modeling (KIRMAT) of spring and deep borehole water compositions in the small granitic Ringelbach catchment (Vosges Mountains, France)

Y. Lucas*, F. Chabaux, T. Schaffhauser, B. Fritz, B. Ambroise, J. Ackerer, A. Clément

Laboratoire d'Hydrologie et de Géochimie de Strasbourg (LHyGeS), Université de Strasbourg et CNRS, 1 rue Blessig, 67084 Strasbourg, France

ARTICLE INFO

Handling editor: Prof. M. Kersten.

Keywords:
Spring waters
Borehole water
Hydrogeochemical modeling
Granitic weathering
Critical zone
Research catchment

ABSTRACT

This study presents the results of the coupled hydrogeochemical modeling of the geochemical compositions of spring and borehole waters from the Ringelbach catchment, which is located in the Vosges Mountains (France). This site has been equipped with 150-m-deep boreholes, facilitating the sampling of both rock and groundwater in the granitic bedrock. The data point to very contrasting chemical compositions between spring and borehole waters, which are discussed and explained in this study by the application of the coupled hydrogeochemical code KIRMAT. Using hydrological and geochemical data, simulations were performed through two different water pathways, which crossed different types of rocks within the Ringelbach massif: a subsurface and fast (> 2.5 $m_{H2O}.yr^{-1}$) water flow, which is more or less parallel to the slope, for waters supplying the springs, and a rather vertical and slower flow (0.5–0.1 $m_{H2O}.yr^{-1}$) for the borehole waters. The KIRMAT simulations make it possible to account for not only the geochemical differences between the spring and borehole waters but also the geochemical variations observed in waters in both contexts. For borehole waters, the model confirms the importance of the dissolution of minor mineralogical phases that are present in the granite (here, carbonates/dolomites) on the chemical budget of waters. It also shows that the chemical differences between the waters collected in the two studied boreholes result from differences in the water flow in the granitic bedrock, i.e., the difference between water flow in a regular porous medium and water flow in a porous medium crossed by a fracture. This result likely highlights the role of geological inheritance on the hydrodynamical rock properties and the chemical compositions of waters circulating within the granitic bedrock. For spring waters, this model enabled us to constrain the nature of the rock in the pathway, which is neither saprolite nor fresh granite but is instead weathered granite with a weathering age of several tens of thousands of years. Spatial and seasonal variations in the chemical compositions of spring water can be explained as the result of the same circulation pattern for which the water-rock interaction time is determined by the length of the pathway and the water velocity. Especially in cases in which this interaction time is long enough, the precipitation of clay phases is enabled, which plays a major role in determining the chemical composition of the water. Despite the only one-dimensional approach and the uncertainties linked to the geochemical complexity and the associated kinetic data, the results obtained in this study demonstrate the effectiveness of using coupled hydrogeochemical modeling to better understand and quantify the weathering processes and the coupling that exists between water circulation dynamics and water-rock interactions at the catchment scale.

1. Introduction

The weathering processes controlled by water-rock interactions at the interface between atmosphere, hydrosphere, biosphere and lithosphere, the so-called "critical zone", are key drivers of the evolution of continental surfaces, which ultimately control the nature and quality of soils and waters (e.g., Banwart et al., 2011; Brantley et al., 2007). Characterizing and modeling these processes, by taking into account their possible diversity, is therefore a major scientific challenge in understanding the evolution of the critical zone and predicting its responses to environmental changes. This is undoubtedly also an essential step in developing the sustainable use of water and soil resources.

These challenges certainly explain the effort currently being made by the scientific community to decipher the main mechanisms controlling the evolution of the critical zone, including the development of geochemical tracing and hydrogeochemical modeling approaches (e.g.,

* Corresponding author.
E-mail address: ylucas@unistra.fr (Y. Lucas).

http://dx.doi.org/10.1016/j.apgeochem.2017.10.005
Received 30 May 2017; Received in revised form 9 October 2017; Accepted 12 October 2017
Available online 14 October 2017

Chabaux et al., 2017). Such studies and their associated developments benefit from the use of well-instrumented/monitored research sites, where the various components involved in the functioning of the critical zone can be studied. The analysis of such research sites should make it possible to better identify the different components involved in the evolution of continental surfaces and, in particular, to better understand the vertical extension of the zone that is impacted by the circulation of water in the substratum.

This is the aim of this study. This work focuses on the geochemical analysis and coupled hydrogeochemical modeling of the waters of the Ringelbach research catchment located in the Vosges Mountains, France. Interdisciplinary studies of the structure and functioning of the main components of the water cycle in this temperate middle mountain environment have been conducted since 1975 (Mercier, 1982; Ambroise, 1995, 2016; Baltassat et al., 2005; Schaffhauser et al., 2014). In addition to the large range of data sets that are available, this site is ideal for such a study because it has been equipped with 150-m-deep boreholes, thus allowing us to sample borehole waters in the granitic profile in addition to spring waters. The Ringelbach catchment is therefore a very suitable site for evaluating the diversity of the weathering processes in relation to different water pathways. This study uses the multi-component reactive transport model KIRMAT [Kinetic Reactions and Mass Transfer] (Gérard et al., 1996, 1998) to characterize the nature of the water-rock interactions controlling the chemical composition of the Ringelbach waters. The advantage of KIRMAT is that it is able to take into account clay phases, whose precipitation plays an important role by drawing down the solute concentration and, thus, preventing the equilibrium of primary minerals (Ganor et al., 2007; Maher et al., 2009).

2. Materials and methods: site description and samples

2.1. Site description

The Ringelbach catchment is a small research catchment (0.36 km^2) located at Soultzeren (Haut-Rhin), on the eastern side of the Vosges massif (North-Eastern France) (Fig. 1). Its elevation ranges from 1000 m to 750 m, resulting in a temperate middle mountain climate, with mean annual temperature, precipitation and potential evapotranspiration values of about 7.5 °C, 1250 mm yr^{-1} and 600 mm yr^{-1} respectively at 800 m (Ambroise, 1995). Its bedrock is a Hercynian porphyritic granite capped in its upper part by a residual cover of Triassic sandstones. The porphyritic granite is medium-grained, relatively homogeneous, rich in biotite, and made of quartz, plagioclase, K-feldspar and amphibole (Gagny, 1968; Wyns, 2012). The Triassic sandstone cover, which gently dips towards the north, is composed of relatively thick, hard, medium-grained sandstone layers interstratified with a series of thinner beds of relatively fine, clayey and indurated sand.

This sandstone covers a 20- to 35-m-thick upper layer of loose, relatively clayey saprolite, which mainly contains granitic sand and gravel and Mn-Fe oxy-hydroxides. The induration and foliation of this truncated saprolite layer increase at its bottom. It overlies a very thick layer of relatively fissured, weathered granite. This succession of subhorizontal layers is interpreted to reflect a truncated pre-Triassic stratified weathering profile of the Hercynian granite (Wyns, 2012), as has also been proposed in other European Hercynian regions (Wyns et al., 2004). Because of this typical weathering profile, hard-rock aquifers typically consist of a capacitive zone in the slightly permeable saprolite and a transmissive zone in the fissured granite (Maréchal et al., 2003).

Analyses of three boreholes (F-HUR, F-HEI, F-HEI2) drilled in 2005 at the Hurlin (965 m) and Heidenkopf (940 m) sites, whose characteristics are presented in Fig. 1, have confirmed the multi-layer structure of the Ringelbach substratum (Wyns, 2012). The deep borehole F-HUR (150 m deep) was cored over its entire length, and F-HEI (150 m deep) was only cored in the lower 50 m of the borehole within the fissured/weathered granite.

Two faults divide the catchment into three blocks (Bunker, Hurlin, Heidenkopf), which are progressively downthrown from southeast to northwest. Within each block, periglacial and postglacial weathering and erosion processes have generated more recent regolith on slope surfaces, which is typically only about few meters thick.

The coarse-textured soil top layer is very permeable on the whole catchment, allowing fast rainwater infiltration and percolation down to the much less permeable saprolite or the fissured granite. Seven main springs are present on slopes (Fig. 1). One drains the Heidenkopf sandstone aquifer (SRV), and six flow from granite, occurring along an altitudinal profile: five of them on the Hurlin/Bunker fault (SH, 915 m a.s.l.; SRH, 880 m a.s.l.; SP2M, 830 m a.s.l.; SPUI, 800 m a.s.l.; SCLS, 750 m a.s.l.), the sixth one at mid-slope on the Hurlin block covered by sandstone (SAH, 850 m a.s.l.).

2.2. Water sampling and analysis

Borehole water samples were collected in both sandstone (F-HEI2) and granite (F-HEI, F-HUR) aquifers. Sampling was performed in 2008–2010 after the complete renewal of borehole water at several depths within the water column in each borehole, using a 1-L acrylic sampler ISMA. Three series were collected in F-HUR (60, 75, 90, 120 and 140 m b.s), five series were collected in F-HEI2 (45 and 55 m b.s), and five series were collected in F-HEI (80, 110 and 140 m b.s.). Samples were also collected during two pumping operations in F-HEI. Springs were sampled from 2001 to 2003 during significantly contrasting hydrological conditions and were also sampled monthly over two hydrological years from October 2004 to September 2006. On each sampling date, the water discharge was measured at the SPUI, SP2M and SRV springs. The temperature of all samples was measured on the field; it is between 8.2 and 9.9 °C.

Analytical techniques (i.e., using a Mettler DL40GP Memotitrator for alkalinity; a Perkin-Elmer 430 spectrometer for Na^+, K^+, Ca^{2+}, Mg^{2+}; and a Dionex Ion Chromatograph for Cl^-, NO_3^-, SO_4^{2-}) used to determine the chemical compositions and pH at laboratory of these water samples. The presentation of the results is detailed in Schaffhauser et al. (2014) and partially reproduced in Appendix B. The compositions of the samples are used as references for comparison with simulation results.

2.3. Rock mineralogy

A previous study characterized the petrography of the fissured zones along these two borehole profiles using macroscopic and microscopic observations (Wyns, 2012). The present study is mainly focused on both the “fresh” and “weathered” granites. Thus, 11 core samples were collected along the F-HUR profile: 3 in the saprolite, 6 in the relatively fresh granite, one in a brecciated zone and one in a fissured zone filled by carbonates. In addition, 4 core samples of the more fissured weathered granite were collected in the F-HEI profile. Rock samples were dried at 110 °C before undergoing calcination at 1000 °C to evaluate wetness and loss on ignition. After alkali fusion, the concentrations of major and trace elements were determined using inductively coupled plasma atomic emission spectrometry (ICP-AES) and inductively coupled plasma mass spectrometry (ICP-MS), respectively. A total of 50 mg of calcinated samples were mixed with lithium tetraborate with a sample/flux ratio of 7.5 and placed in an oven at 1000 °C for 30 min under a controlled Ar atmosphere. The fusion residue was then dissolved in a nitric acid solution (Samuel et al., 1985). The overall analytical uncertainty is < 3% (± 2σ) for major element concentrations and < 10% (± 2σ) for trace element concentrations.

The modal mineralogies of the “fresh” granite and the saprolite have been estimated by norm calculations. This technique uses the chemical compositions of the rocks and minerals determined by X-ray diffraction analyses of the whole rocks in the F-HUR borehole profile (Schaffhauser et al., 2014) (Appendix A). For this calculation, the chemical

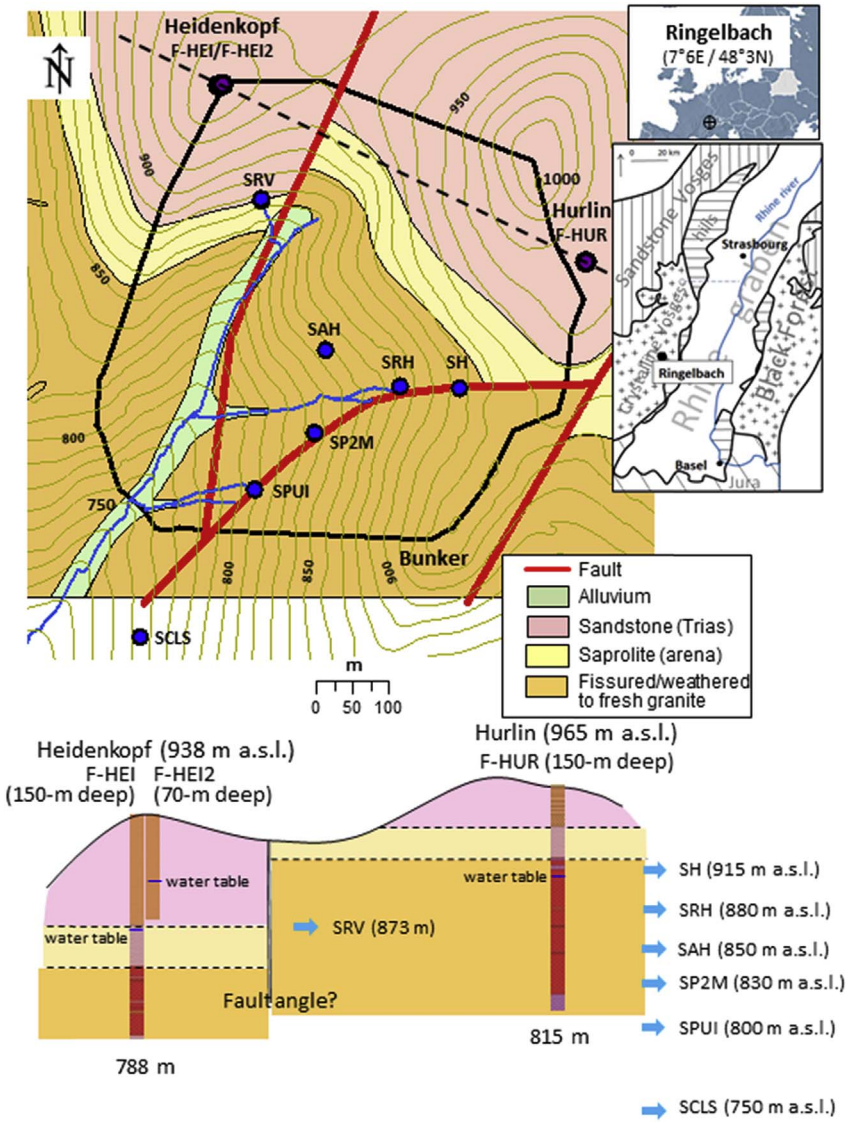

Fig. 1. Topographic and geologic map of the Ringelbach catchment with the locations of the sandstone spring (SRV), granitic springs (blue circles) and boreholes (F-HUR, F-HEI, F-HEI2). The dotted line indicates the position of the geological section presented below. F-HUR borehole: 150 m deep, through sandstone (0–28 m b.s.), saprolite (28–48 m b.s.) and fissured granite; cored full length, casing down to 51 m b.s.; very low transmissivity; water table depth (granite aquifer): 61.5 m b.s. ± 1.5 m. F-HEI borehole: 150 m deep, through sandstone (0–74 m b.s.), saprolite (74–101 m b.s.) and fissured weathered granite; cored below 101 m b.s. only, casing down to 101 m b.s.; water table depth (granite aquifer): 77 m b.s. ± 1 m; rather high transmissivity only because of a draining fracture intersected at 131 m b.s. (Lods et al., 2011). F-HEI2 borehole: 70 m deep, in sandstone only; not cored, full length perforated casing; rather low transmissivity; water table depth (sandstone aquifer): 45–50 m b.s. with rapid formation of peaks up to 25 m b.s.. From Schaffhauser et al. (2014). (For interpretation of the references to colour in this figure legend, the reader is referred to the web version of this article.)

composition used for each mineral comes from chemical analyses of the "*granite des crêtes*" (Gagny, 1968) and/or from microsonde analysis performed on some granitic core samples collected in the Ringelbach catchment (Wyns, 2012).

Several approximations were made in the norm calculations. The plagioclase solid solution was separated into proportions of their pure end-members (albite and anorthite). The proportions of amphibole and biotite were calculated by making the assumption that all titanium and magnesium are incorporated into these two minerals, using the method proposed by Nicolas (1966). When the calculation does not allow the coexistence of the two phases, only biotite is assumed to be present, as it is preponderant in the granitic rocks. To define the mineralogy of a fresh granite, the amounts of secondary phases in porphyritic granite sampled in the F-HUR borehole were considered to be negligible and were not taken into account in the norm calculations. If X-ray diffraction detected dolomite, a volume proportion of 1% of dolomite was considered as a first approximation. Indeed, a proportion greater than 2% does not permit the formation of any other mineral containing calcium (i.e., amphibole and anorthite). The calculation of the carbonate proportion in the fissured zone, which is rich in calcite and dolomite, is based on the assumption that the loss on ignition is exclusively due to the calcination of carbonate.

In the saprolite layer, the amount of clay minerals cannot be neglected. The estimations of the diffraction peak areas for fine particles (< 2 μm) were obtained by using the program MacDiff 4.2 (Petschick, 2000), which allowed us to quantify the proportions of clay phases present in this fraction (Duplay et al., 2014). The relative proportion of each clay phase was therefore determined by extrapolating the ratios of clay proportions found for fine particles to the whole rock and taking into account the classical structural compositions of kaolinite ($Si_2Al_2O_5(OH)_4$), smectite ($Si_{3.83}Al_{1.84}Mg_{0.38}O_{10}(OH)_2K_{0.4}$) and illite ($Si_{3.5}Al_{2.3}Mg_{0.25}O_{10}(OH)_2K_{0.6}$). The calculated norms are presented in Supplementary Table S1.

2.4. Rock hydrodynamical properties

The variations of rock porosity and permeability with depth were estimated from the available data sets derived from core sample measurements at laboratory: 57 for porosity and 24 for permeability along the F-HUR profile, and 6 for porosity and 1 for permeability on the F-HEI profile (Baltassat, 2017; Haceb, 2006; Schaffhauser et al., 2014). These data are given in Appendix C. As no data are available at field scale, these are the mean values of core measurements that have been used in the simulations.

3. Hydrological and hydrochemical functioning

Because of the presence of very permeable, coarse-textured soil top layers (Ambroise and Viville, 1986; Viville et al., 1986), no runoff is observed on the slopes, even during periods of high-intensity rainfall. Rainwater infiltrates into the soil and may percolate vertically within the much less permeable regolith, thus possibly generating a transitory lateral subsurface stormflow downslope during high flow events. A detailed study of the chemical and isotopic compositions of the catchment waters (Schaffhauser et al., 2014) showed that spring waters are mainly supplied by relatively shallow subsurface waters flowing through water paths that are completely different from those of deeper borehole waters.

As well exemplified in the alkalinity vs pH diagram (Fig. 3) and as already discussed in the study of strontium isotopic ratios by Schaffhauser et al. (2014), the measured geochemical data of the Ringelbach waters point to clear chemical differences between the spring waters group and the borehole waters group. In addition, there are systematic differences between both boreholes (Figs. 3 and 4): for example, F-HUR waters are more concentrated than F-HEI waters and exhibit a dispersion due to small seasonal variations. In the borehole waters, this chemical contrast between F-HUR and F-HEI waters can be linked to different water pathways for their input waters collected in the two boreholes. The F-HEI water supply is indeed highly controlled by a sub-vertical fracture intersected at a depth of 132 m, which can provide a high water flux during pumping (Lods et al., 2011). There is no such short-circuiting fracture in F-HUR.

Waters of the several springs located at varying altitudes along the Hurlin/Bunker fault present large space and time variations in both flow quantity and quality (Schaffhauser et al., 2014). Spring water discharges and concentrations increase downslope as an effect of increasing supply area and contact time with rock. In addition, waters of each spring are affected by seasonal variations, with measured concentrations decreasing from low to high flow conditions (Fig. 8).

4. Modeling strategy

All these previous findings suggest a rather close control of hydrological parameters on groundwater chemistry and the nature and intensity of the weathering processes involved in the Ringelbach substratum. To test this assumption, quantify and explain the resulting effects, water-rock interactions have been simulated using the KIRMAT coupled hydro-geochemical modeling code. As very little information is available on rock characteristics, only measured water chemical data sets (available in supplementary data in Schaffhauser et al., 2014 – see also Appendix B) have been used to validate the modeling procedure, as well as to calibrate some unknown or poorly known rock parameters.

4.1. The KIRMAT code and its functionalities

The Eulerian thermokinetic hydrochemical code KIRMAT (Gérard et al., 1998a,b) was developed from the single-reaction path model KINDIS (Madé et al., 1994), by using its geochemical formulation and numerical method to solve chemical equations. The thermokinetic geochemical code KINDIS was developed from the purely thermodynamic code DISSOL (Fritz, 1975, 1981, 1985; Fritz and Tardy, 1976), which in turn originated from PATH1 (Helgeson et al., 1970). Theoretical kinetic rate laws for mineral dissolution and precipitation based on the Transition State Theory (TST) were implemented in DISSOL in order to create KINDIS. One of its strengths is that it addresses clays as solid solutions with variable compositions (Tardy and Fritz, 1981). These geochemical codes have been numerically tested and used in studies of hydrothermal, diagenetic, nuclear waste storage and weathering processes (e.g., Bertrand et al., 1994; Noack et al., 1993; Marty et al., 2010; Lucas et al., 2010; Schaffhauser, 2013).

The KIRMAT modeling is one-dimensional, the parameters and imposed conditions required for each simulation are: (i) for fluid: input water composition and flux (Darcy's velocity), initial water composition, redox and pCO_2; (ii) for rock: total porosity, reactive surface area, kinetic dissolution rate constant, and initial proportion of each mineral and secondary phase to be tested. Among the available functionalities, the feed-back effects of dissolution and precipitation on porosity and reactive surface area were used.

4.2. Estimated hydrodynamical parameters and water pathways

To estimate the main water fluxes flowing within the structured bedrock, which control its weathering and must therefore constraint KIRMAT simulations, a hydrogeological 2D model described in Appendix D has been developed using the software COMSOL (Pryor, 2011). It is necessarily simplified as actual hydrogeological characteristics are poorly known. It allows for the identification of two main pathways for groundwater and the estimation of water fluxes at steady-state: (a) a downslope, near surface, relatively fast water flow supplying the springs within the regolith, with two estimations of the downslope flux: average value of 9 $m_{H2O}.yr^{-1}$ (mean flow conditions) derived from the hydrogeological model, and an lower value of 2.5 $m_{H2O}.yr^{-1}$ (low flow conditions) estimated in Schaffhauser et al. (2014) from the variation of the U activity ratios within spring waters at low-flow periods; (b) a vertical and slower water flow with fluxes of about 0.5 $m_{H2O}.yr^{-1}$ in the saprolite and 0.1 $m_{H2O}.yr^{-1}$ in the granite, for the deep waters. The simulation also shows that most of the water circulating within the massif is drained by near surface flow (Ambroise et al., 1996). Because of the intersected supplying subvertical fracture (Lods et al., 2011), it is assumed that the vertical flux around F-HEI is not smaller than in the saprolite, i.e. much greater than around F-HUR (0.5 $m_{H2O}.yr^{-1}$ and 0.1 $m_{H2O}.yr^{-1}$, respectively).

All of these considerations allow us to build the conceptual one-dimensional scheme shown in Fig. 2 to model the geochemical compositions of the borehole and spring waters in the Ringelbach catchment and their spatial variation. It consists in four different columns of different lengths, each discretized into boxes and assumed to be initially homogeneous for both rock and water characteristics: three vertical columns, with a saprolite column connected at its bottom to either a F-HUR granite column or a F-HEI granite column for simulating borehole profiles, one separate sloping column for the regolith layer assumed to supply springs.

It is worth noting that using such a 1D model leads to an approximation of the actual 2D or 3D functioning of the sloping regolith layer. In particular, it does not allow taking explicitly into account the specific hydrological and geochemical effects of the actual vertical atmospheric recharge all along the slope and its progressive accumulation downslope.

4.3. Geochemical conditions and parameters

The vertical evolution of the water chemistry in boreholes has been modeled using a succession of boxes intersecting two different lithological zones (Fig. 2). The water entering the saprolite layer is assumed to have the same composition as the water leaving the overlying sandstone cover, as determined by the F-HEI2 sandstone water sample collected at a depth of 55 m (Schaffhauser et al., 2014). When defining the initial composition of the water in rock, the results of preliminary modeling indicated that its precise composition does not exert a significant impact on the final concentration profile during simulation times that are longer than the water residence time in the column (less than 30 years, based on estimated flux and porosity). Thus, this initial water composition is defined as being equal to that of the entering water. The pH of the sandstone water varies between 6.3 and 6.7 (Schaffhauser et al., 2014) and a redox potential Eh of +250 mV is imposed, which is a value characteristic of an intermediate medium between atmospheric water and isolated groundwater (Garrels and

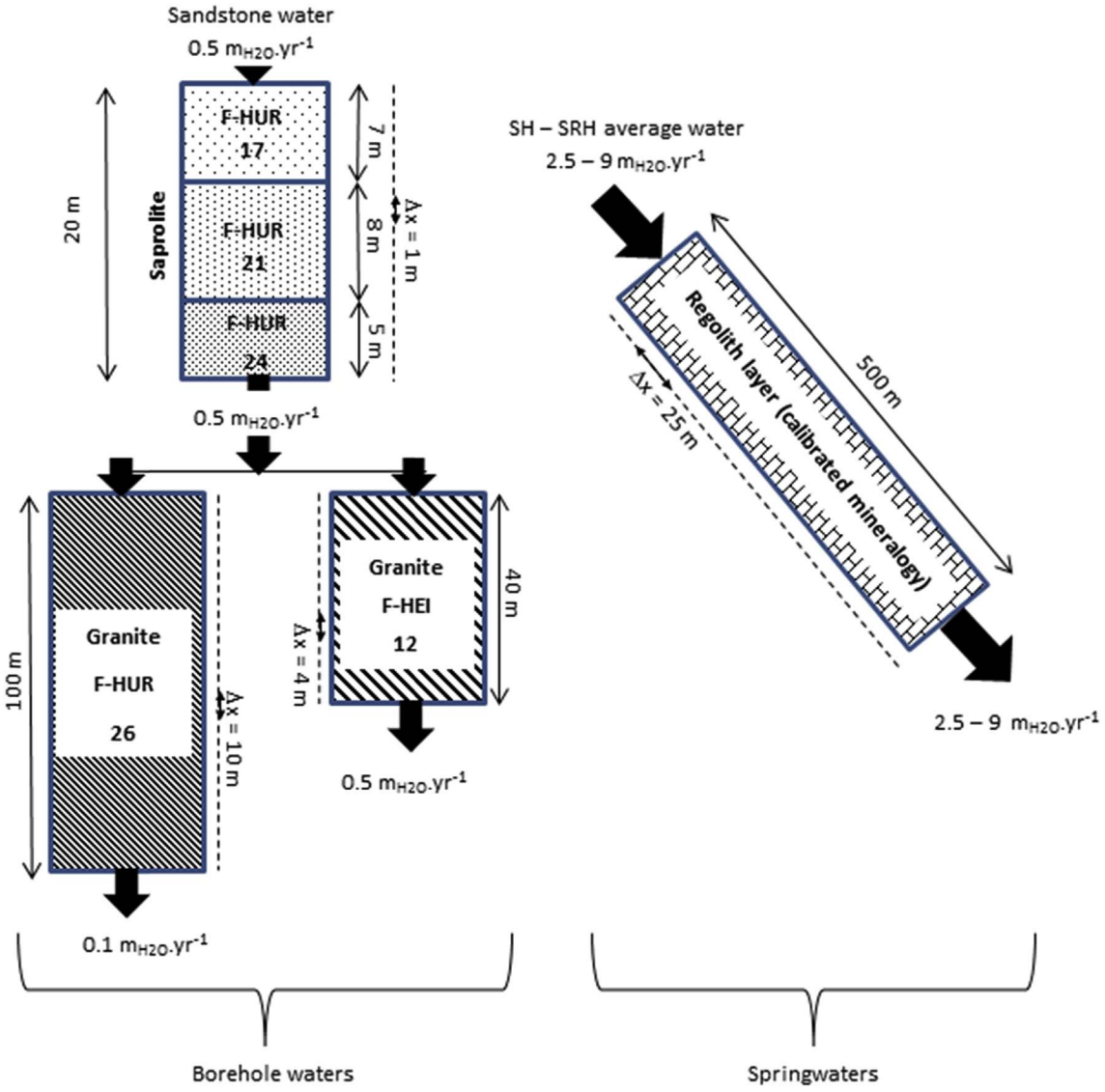

Fig. 2. Rock mineralogies, input water fluxes and composition of the 1D columns used in KIRMAT simulations. To model the geochemical compositions of spring and borehole waters, two main water pathways were retained: the first one is vertical for the deep waters; the second one is subparallel to the surface supplying the granitic springs. In simulations, the length of the water pathway is considered to be equal to the geometric length and is discretized in Δx-length meshes.

Christ, 1967). The water flux entering the porphyritic granite has the simulated composition of the calculated water flux leaving a 20-m-thick saprolite.

During all simulations, the partial pressure of CO_2 is assumed to be constant and is set to a value of 10^{-3} atm, based on equilibrium calculations performed using the measured compositions of samples. This value, which is higher than the atmospheric value, is consistent with that of other studies (e.g., Bouma et al., 1997). If, alternatively, a closed environment with a non-constant partial pressure is retained, thus enabling the free variation of pCO_2 as a function of the total carbonate in the solution, then the pH of the simulated water rapidly reaches values close to 10: this is clearly too basic compared to the values measured in the F-HUR waters, which invalidates such a simulation option.

The minerals selected for each layer are tested for the case of kinetically controlled dissolution. The initial mineralogical compositions considered for the 20 m thick saprolite are based on the norm calculations of the three rock samples from this layer (F-HUR17, F-HUR21 and F-HUR24) (Table 1). The saprolite profile is divided into three areas, in which the mineralogical composition of each area corresponds to that of one of the three samples. The porphyritic granite included in F-HUR simulations is considered as a first approximation to be "fresh" and homogeneous along the entire profile, and its mineralogical composition is assumed to be the same as that of the F-HUR26 sample. The granite porosity ω used in the F-HUR simulations is 3%, which is the mean value of the measured porosity in the porphyritic granite (Table 1, Appendix C).

The reactive surface areas of the involved minerals are calculated from a simple geometric pattern based on macroscopic observations of the F-HUR granite rock samples. Minerals are assumed to be cubes with sides that are 1 mm long, except for K-feldspar, which are assumed to be cubes with 1-cm-long sides, and clays, which are characterized by dimensions of 1 μm. The total area of a particle in contact with the solution S_p^{total} (m^2/kg_{H2O}) is thus recalculated from the following equation used for porous media:

$$S_p^{total} = V_p * \frac{S_{cube}}{V_{cube}} \quad (1)$$

where Vp is the volume of the mineral per kilogram of water ($m^3.kg^{-1}$), and S_{cube} and V_{cube} are the surface and volume of the cube, expressed in m^2 and m^3, respectively. Vp is calculated using:

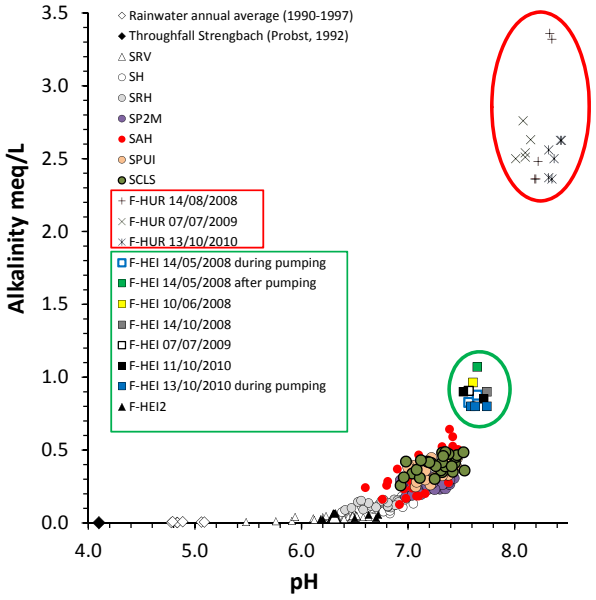

Fig. 3. Measured alkalinity vs pH for boreholes and springs water samples.

$$V_p = X_p * \frac{(1-\omega)*1000/\rho}{\omega} \quad (2)$$

where X_p is the volume fraction of the mineral, ρ is the fluid density ($kg.m^{-3}$), and ω is the porosity. The calculated values of the reactive surface areas of minerals are presented in Table 2.

The mineralogical, physical and hydrodynamic properties of the porphyritic granite in F-HEI are very different from those in F-HUR. According to observations and results obtained by the characterization of core samples, the F-HEI granite is more weathered and fractured than the F-HUR granite. In addition, the F-HEI borehole is characterized by high transmissivity, as its water is essentially supplied by an open fracture located at a depth of 132 m (Lods et al., 2011). Therefore, the mineralogical composition of the granite used is that of sample F-HEI12, which is the closest to this fault zone (Table 3). This sample is considered as the most representative of the local granite in the weathering zone along the water-supplying fracture. A granite porosity of 9% is used for the F-HEI simulation, based on its porosity measurements. The total reactive surface area of the more fractured F-HEI granite is approximated by two parallel fracture planes separated by 1 cm, which from Madé (1991) leads to a value of $0{,}1 m^2/kg_{H2O}$, much smaller than for F-HUR granite (Table 3).

The X-ray diffraction analysis of cuttings has also confirmed the presence of smectite and illite, which were observed in samples of F-HUR and F-HEI granites (Appendix A). However, the exact structural formulas of these clays are not known. A solid solution of 15 end-members was used to simulate the precipitation of clay and to model their chemical compositions during the weathering process in the simulations. These solid solutions were constructed to define a wide range of possible clay mineralogical compositions. The end-members and their thermodynamic equilibrium constants are given in Table 4.

On the basis of hydrological and petrological data, it is difficult to estimate the time at which the “deep” weathering system began to operate in its present configuration. Nevertheless, on the basis of the interpretations of Wyns (2012), we assume that the saprolite/granite succession observed in these profiles reflects an inheritance of the pre-Triassic weathering of the granite, which was partly truncated by erosion prior to the deposition of Triassic sandstone. Furthermore, Schaffhauser et al. (2014) proposed, based on weathering rates deduced from the isotopic variations of uranium in springs and an empirical relationship defined by Maher et al. (2006, 2009), that the weathering of the Ringelbach substratum in its present structure could have begun several hundreds of thousands of years ago. We chose to simulate the weathering of the profile over a period of 10,000 years in its current structure by simulating flow using F-HUR 26, which is the least weathered sample available to us, as the initial rock.

To simulate the compositions of spring waters, we used an input water composition with an average composition of waters from the SH and SRH springs. Indeed, although SH is at a higher elevation, a previous study (Schaffhauser et al., 2014) showed that SRH, which is lower than SH, can better represent the origin of spring water in a one-dimensional model. Through the calibration procedure, this average value between SH and SRH was estimated to be the best input water to account for the composition of the springs. In the absence of mineralogical and petrophysical data on the regolith crossed by the spring waters, mineralogical data of the rock sample F-HUR26, with a porosity of 3%, were extended to the slope length and used to simulate spring waters. As no information is available for water composition in regolith, the initial water was chosen equal to input water. A ten-year simulation period has been chosen to ensure quasi stationary regime.

Preliminary simulations performed using published dissolution rates (Table 5) led to an overestimation of cations concentrations. Hence, we adjusted these parameters: for borehole waters, by dividing the dissolution rates of biotite (Bray et al., 2015) and albite by 50 to control the concentrations of potassium and sodium, respectively, and dividing the dissolution rates of other minerals by 10 to control the concentrations of calcium and magnesium; for spring waters by dividing all dissolution rates by 10. These adjusted dissolution rates, which remain within the ranges proposed by other authors (e.g., Palandri and Kharaka, 2004; for minerals other than amphibole), have been used for all simulations.

Such a drastic reduction of the dissolution rates seems consistent with the fact that rates measured in the laboratory are often several orders of magnitude higher than those estimated in natural systems (Maher et al., 2006): see for instance Velbel (1993), Taylor et Blum (1995) and White and Brantley (2003) for silicate minerals in general, Kim (2002) for plagioclase, and Brantley et al. (1993) for feldspar and hornblende. Furthermore, uncertainty exists about the effective reactive surface of minerals in contact with water, which depends on the structure of the porous medium (Zhu, 2005), and the mineralogical organization within the medium. And in the Ringelbach case, this structure of the porous medium is different for the rather deep flows in granite relative to borehole waters and the relative surface flows in regolith relative to spring waters, which could contribute to explain the differences between dissolution rate values used for borehole or spring waters.

5. Results and discussion

5.1. Modeling of the F-HUR borehole water chemical composition

We note that weathering simulations performed over 1000 years (not shown), 5000 years 10,000 years or 20,000 years (Fig. 10a) yield very similar results (also for F-HEI, not shown), which means that the 10,000 year weathering duration leads to a weathered system in a relatively stationary state. The simulated values of alkalinity vs pH and Na, Ca, Mg, K vs H4SiO4 concentrations are very consistent with the measured values in the F-HUR waters (Fig. 4).

In the saprolite, the simulated final molar quantities of destroyed minerals are low, which is consistent with the fact that the most alterable minerals have been largely dissolved in the already strongly weathered horizon. After 10,000 years of simulated weathering, only 0.8% of anorthite, 0.1% of albite and biotite and less than 0.1% of potassium feldspar were dissolved. The simulated solution is also undersaturated with respect to the clay minerals that are present in the saprolite, such as montmorillonite and illite. The amounts of destroyed

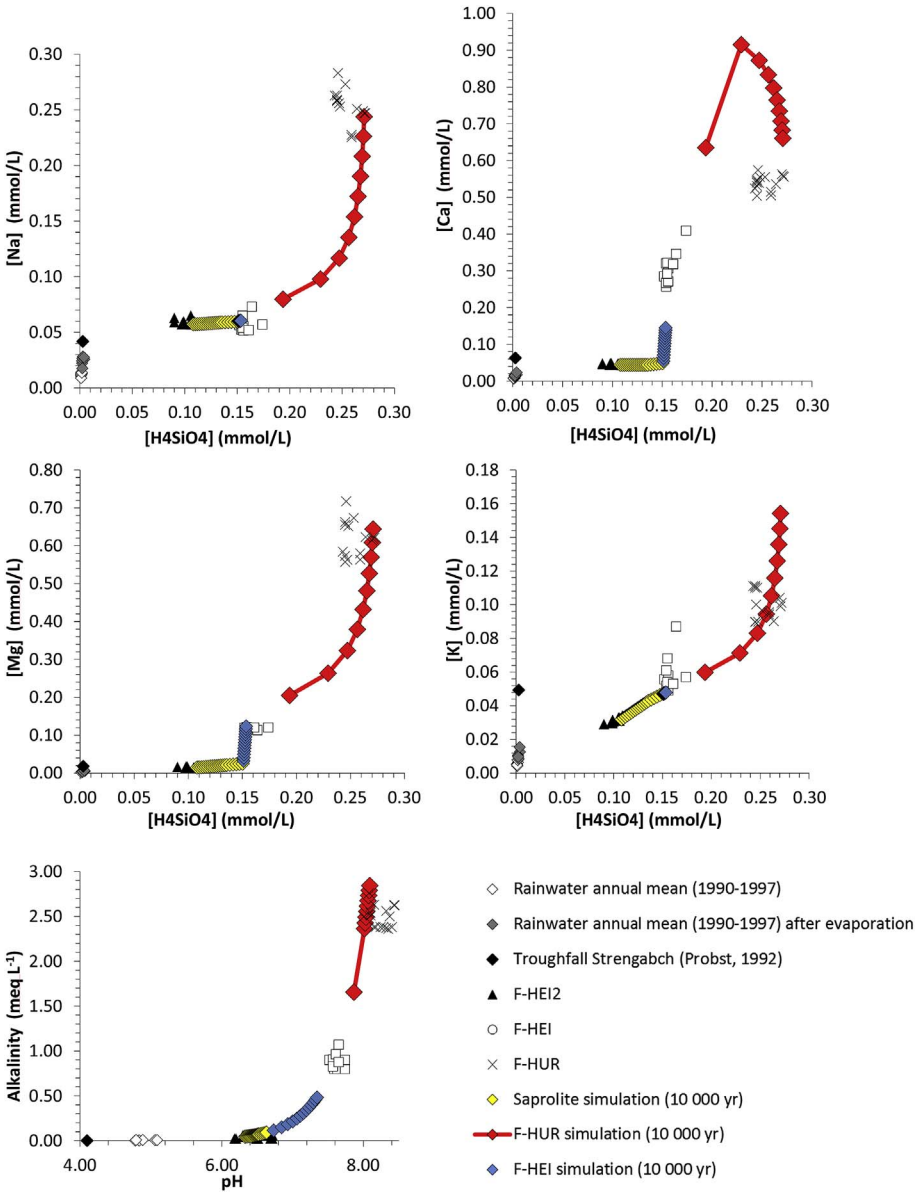

Fig. 4. Comparison of measured and simulated concentrations of boreholes waters after 10,000 years of weathering. Ten simulation boxes per profile. Simulated concentrations increase with increasing depth.

Table 1
Mineralogical compositions (% volume) used in F-HUR simulations.

Volume fraction (%)	Granitic saprolite			"Fresh" porphyritic granite F-HUR
Minerals	F-HUR17 (porosity 16.5%)	F-HUR21 (porosity 10.6%)	F-HUR24 (porosity 10.6%)	F-HUR26 (porosity 3%)
Quartz	32.4	27.6	29.5	25.4
K-Feldspar	16.6	29.4	26.8	27.5
Albite	5.6	6.1	5.7	14.9
Anorthite	0.0	0.0	0.6	6.6
Biotite	9.6	15.6	15.0	21.0
Amphibole	0.0	0.0	0.0	2.2
Apatite	0.2	0.3	1.3	1.2
Hematite	3.4	1.4	0.9	0.2
Dolomite	0.0	0.0	0.0	1.0
Kaolinite	3.7	2.3	0.3	0.0
Illite	27.0	15.9	10.8	0.0
Montmorillonite	1.6	1.3	9.1	0.0

minerals reached values of 0.8% and 0.3%, respectively, after 10,000 years of weathering. These results also indicate that the sandstone water composition evolves slightly along the saprolite profile. Among the secondary minerals, only kaolinite and hematite reach thermodynamic equilibrium and precipitate in this part of the profile. These low dynamics explain the quasi-stable evolution of the simulated porosity, which remains approximately constant near the measured value of 16.5% (Appendix C), at the top of the profile after 10,000 years of weathering.

In the porphyritic granite, the simulated final destroyed molar proportions over 10,000 years amounted to 8% for anorthite, 2% for amphibole and 0.1% for albite and biotite (Fig. 5). The dolomite, which was initially super-saturated in the solution throughout the profile, becomes undersaturated in the upper 10 m of the porphyritic granite. Characterized by its high reactivity, the dolomite is dissolved down to 20% at the top of the profile of the porphyritic granite. In the final volume of mineral precipitates, it represents less than 1% of the total volume.

Table 2
Calculated reactive surface area *Sp* ($m^2.kg_{H2O}^{-1}$) values for minerals used in F-HUR simulations.

Computed reactive surface *Sp* ($m^2.kg_{H2O}^{-1}$)	Granitic saprolite			"Fresh" porphyritic granite F-HUR
Minerals	F-HUR17 *Sp* ($m^2.kg_{H2O}^{-1}$)	F-HUR21 *Sp* ($m^2.kg_{H2O}^{-1}$)	F-HUR24 *Sp* ($m^2.kg_{H2O}^{-1}$)	F-HUR26 *Sp* ($m^2.kg_{H2O}^{-1}$)
Quartz	9.84	13.99	14.91	49.28
Albite	1.70	3.07	2.89	28.91
K-Feldspar	0.50	1.49	1.36	5.34
Anorthite	0.00	0.00	0.31	12.80
Biotite	2.91	7.87	7.60	40.74
Amphibole	0.00	0.00	0.00	4.27
Apatite	0.06	0.14	0.65	2.33
Hematite	1.03	0.70	0.46	0.39
Dolomite	0.00	0.00	0.00	1.94
Kaolinite	561.73	592.11	76.93	0.00
Illite	4099.09	4035.52	2727.29	0.00
Montmorillonite	242.91	338.24	2310.96	0.00
Total	4919.00	4993.00	5143.00	146.00

Table 3
Mineralogical compositions (% volume) and reactive surface area *Sp* ($m^2.kg_{H2O}^{-1}$) values for minerals used in F-HEI simulations.

F-HEI weathered and fissured granite (porosity = 9%)		
Minerals	Volume fraction (%)	Calculated reactive area S_p ($m^2.kg_{H2O}^{-1}$)
Quartz	30.4	0.0304
K-Feldspar	31.8	0.0318
Albite	6.0	0.0060
Biotite	1.3	0.0013
Apatite	0.6	0.0006
Iron Oxides	0.8	0.0008
Illite	23.9	0.0239
Kaolinite	2.6	0.0026
Dolomite	1.0	0.0010

Table 4
Solubility product (K) values for the end-members used in the clay solid-solution from KIRMAT database (Fritz, 1981).

Minerals	Structural formula	Log K (25 °C)
Pyrophyllite	$Si_4Al_2O_{10}(OH)_2$	−45.489
Talc	$Si_4Mg_3O_{10}(OH)_2$	25.162
K-Muscovite	$Si_3Al_3O_{10}(OH)_2K$	−53.169
Fe3-Pyrophyllite	$Si_4Fe_2O_{10}(OH)_2$	14.028
Ca-Muscovite	$Si_3AlAl_2O_{10}(OH)_2Ca_{0.5}$	−52.436
Mg-Muscovite	$Si_3AlAl_2O_{10}(OH)_2Mg_{0.5}$	−52.436
Na-Muscovite	$Si_3AlAl_2O_{10}(OH)_2Na$	−52.363
Ca-Ferrimuscovite	$Si_3AlFe_2O_{10}(OH)_2Ca_{0.5}$	4.606
Mg-Ferrimuscovite	$Si_3AlFe_2O_{10}(OH)_2Mg_{0.5}$	4.606
K-Ferrimuscovite	$Si_3AlFe_2O_{10}(OH)_2K$	3.873
Na-Ferrimuscovite	$Si_3AlFe_2O_{10}(OH)_2Na$	4.679
Ca-Phlogopite	$SI_3AlMg_3O_{10}(OH)_2Ca_{0.5}$	19.371
Mg-Phlogopite	$Si_3AlMg_3O_{10}(OH)_2Mg_{0.5}$	19.371
K-Phlogopite	$Si_3AlMg_3O_{10}(OH)_2K$	18.638
Na-Phlogopite	$Si_3AlMg_3O_{10}(OH)_2Na$	19.444

Clay solid solution and calcite reach equilibrium in solution and precipitate deeper in the porphyritic granite (Fig. 6). The fact that the solid solution contains little Na and K indicates that the concentrations of these elements in solution are mainly controlled by the dissolution rates of primary minerals, namely, biotite for K and albite for Na. In contrast, the simulated concentrations of Si, Mg and Ca in solution depend on both the dissolution rates of the primary minerals containing these elements and the precipitation of the clay solid solution. Calcite precipitation also controls the aqueous Ca concentration.

The precipitation of secondary mineral phases also plays a role in the evolution of porosity profile over 10,000 years of weathering (Fig. 6). In the upper twenty meters below the saprolite layer, the significant dissolution of dolomite combined with the absence of calcite precipitation causes the porosity increase from an initial value of 3% to a value of almost 3.5%. In the lower part of the profile, the combined precipitations of calcite and clay solid solutions tend to close the pores, resulting in a decrease in porosity from 3.5% to 2.9%.

Thus, the simulation results confirm the classical observation that the concentrations of the F-HUR deep waters result from the competition between the dissolution kinetics of primary minerals that release ions in solution and the precipitation of secondary phases that incorporate these elements. This is particularly the case for magnesium, calcium and silica, which are easily incorporated into secondary phases (mainly the solid solutions of clays and calcite). Finally, these simulations confirm the importance of the dissolution of minor phases present in the granite on the chemical budget of waters. This has already been highlighted in another case, the nearby granitic Strengbach catchment, by using isotopic tracing approaches involving Sr and Nd isotopic ratios to determine the effect of apatite on the budget of Sr and Nd (Aubert et al., 2001). This was also demonstrated from the experimental dissolution of granites (White et al., 2005) and mass balance calculations performed at the catchment scale (Oliva et al., 2004). Here, the simulation indicates the significant effect of carbonates, especially dolomite, on the chemical compositions of the F-HUR deep waters. Although the dolomite reaches thermodynamic equilibrium in the profile, its very high reactivity explains the significant amounts of destroyed mineral phases in the uppermost meters of the porphyritic granite (Fig. 5) and the generated increase in porosity (Fig. 6).

5.2. Modeling of the F-HEI borehole water chemical composition

As for F-HUR, graphs of alkalinity vs pH and Na, Ca, Mg, K vs H_4SiO_4 show that the simulated F-HEI concentrations profiles are very consistent with the measured values in F-HEI waters (Fig. 4). And the F-HEI simulations can help to explain the significant differences with F-HUR observed in water composition.

Because the column of porphyritic granite under the saprolite drilled in F-HEI is shorter than that in F-HUR (i.e., 49 m instead of 100 m), the chemical composition of the F-HEI water could simply be explained by its shorter flow path and thus its shorter contact time with the granite. However, according to previous F-HUR simulations (see above), the simulated elemental concentrations in water after following a pathway of 40 m in the porphyritic granite are still too high compared to those measured in the F-HEI waters. Therefore, it is necessary to also consider the geometry and degree of weathering of the granite, which is much more fractured and weathered in F-HEI as explained in chap. 4.3.

The simulated F-HEI solution is undersaturated with respect to the main primary minerals, especially dolomite. The amount of dolomite destroyed along the profile increases upwards, from 25 at the bottom to 35% at the top (Fig. 7). This is mainly the effect of the far lower value of reactive surface area, compared to F-HUR, which maintains the dissolution of this mineral throughout the entire profile. The fact that in F-HEI groundwater flux is higher, so that waters are less concentrated and therefore dolomite reactivity is favored, has been proved to be of secondary importance by numerical testing.

The kinetic constant of dolomite is five orders of magnitude greater than that of silicate minerals, which explains the significant amounts of dolomite destroyed after 10,000 years of weathering. The rapid dissolution of this mineral controls the concentrations of Mg and Ca and the alkalinity of the solution. It also causes a reduction of the reactive surface area over time, which explains the slight decreases in pH, alkalinity and the concentrations of Ca and Mg over time. Conversely, the dissolution rate of the silicate minerals providing Na, K and Si in solution is relatively low. Thus, only 0.01% of albite and biotite are destroyed after 10,000 years of weathering, which explains the very small changes in these concentrations both over time and along the profile.

Table 5
Kinetic data for minerals used in simulations: dissolution rate (k_d) at 25 °C and 10 °C, and activation energy at 10 °C.

Minerals	Log k_d 25 °C (mol.m^{-2}.an^{-1})	Activation energy (kJ.mol^{-1})	Log kd 10 °C (mol.m-2.an-1)
Quartz	−5.502	85.0 (Dove, 1994)	−6278
Anorthite	−3.501	40.0 (Madé, 1991)	−3872
Albite	−4.437	58.6 (Blum and Stillings, 1995)	−4981
K-Feldspar	−5.000	38.0 (Helgeson et al., 1984)	−5.354
Biotite	−4.621	35.0 (Goddéris et al., 2006)	−5.247
Amphibole	−4.031	94.4 (Palandri and Kharaka, 2004)	−4.907
Apatite	−2.686	34.73 (Guidry and Mackenzie, 2003)	−3.009
Dolomite	137.41	34.0 (Pokrovsky et al., 2005)	66.431
Illite	−7.301	14.0 (Köhler et al., 2003)	−7.431
Montmorillonite	−6.871	22.8 (Rozalen et al., 2009)	−7.082
Kaolinite	−5.001	29.3 (Ganor et al., 1995)	−5.273

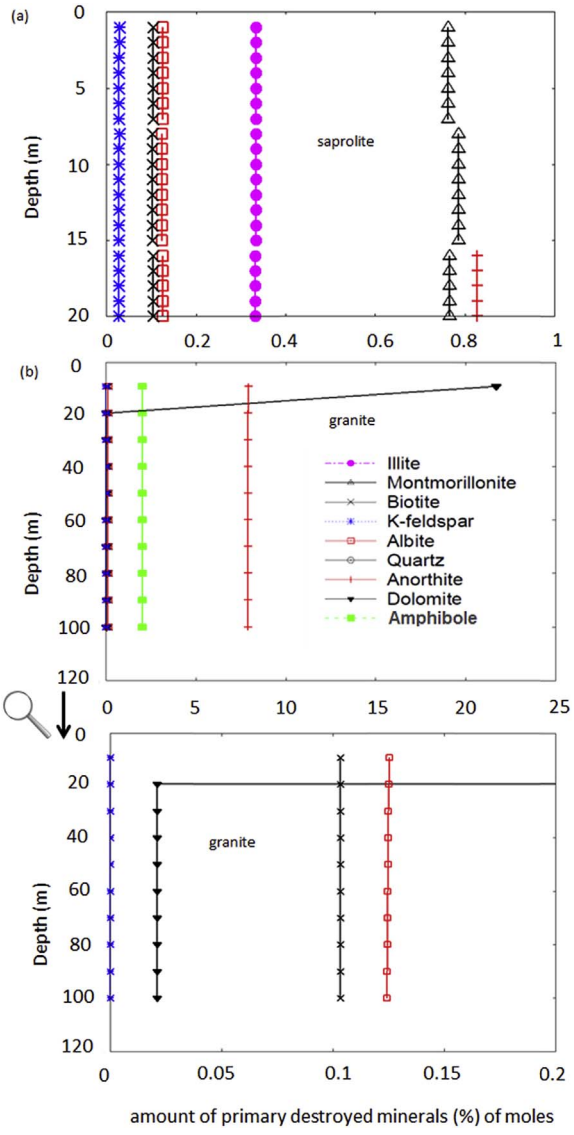

Fig. 5. Simulated final relative proportions (% moles) of minerals destroyed along the F-HUR profile after 10,000 years of weathering: (a) in saprolite, (b) in granite.

Kaolinite and hematite precipitate at thermodynamic equilibrium throughout the profile. The solution remains undersaturated with respect to calcite and solid solutions of clays. The lack of precipitation of these secondary phases explains the small increase in porosity: although initially equal to 9%, the porosity ranges between 9.2 and 9.3% after 10,000 years of weathering.

These simulations show the importance of the geometry of the water circulation on the weathering processes and, in particular, demonstrate the important role that fractures and their associated circulations play. In the case of Heidenkopf, these fractures are related to the tectonic history of the basin (Wyns, 2012). Thus, the structural inheritance of the bedrock controls the localization, nature and intensity of the weathering: only weak weathering is observed at F-HUR, but preferential zones of weathering are linked to fractured rock at F-HEI.

5.3. Modeling of the spring water chemical composition

5.3.1. Calibrated regolith composition

Preliminary simulations were made using the contrasted mineralogies of "fresh" F-HUR granite and saprolite as initial regolith composition. When compared to the water chemistry of granitic springs, simulated final water concentrations were too high using "fresh" granite data and much too low using saprolite data (not shown). The unknown initial regolith composition, which should therefore be intermediate between these two cases, was estimated by calibration on measured spring water data only. The weathering of 1 m^3 of "fresh" F-HUR granite was simulated using KIRMAT (1 single box) over several periods increasing from 10,000 to 100,000 years. The same low water flux of 2.5 $m_{H2O}.yr^{-1}$ and the same physical and chemical data were used as for previous F-HUR simulations. For each weathering period, the final granite composition was then used as initial regolith composition for simulating the whole sloping layer. The 100,000 years weathered F-HUR granite gave the best results when compared to spring water data (Fig. 8) and has therefore been kept as calibrated initial regolith composition (Table 6).

These results further indicate that the water pathway supplying the springs within the watershed is neither situated in the very superficial zone nor in the deep granite but instead at an intermediate depth within the weathered granite. The simulations further allow us to estimate the duration of weathering: it is on the order of several tens to one hundred thousand years. It is worth noting that both of these conclusions are consistent with those deduced from the modeling of variations in the U isotopic ratios within spring waters using a reactive transport model (Schaffhauser et al., 2014).

5.3.2. Influence of residence time on spatial and time variations

The above simulations were performed using two values of input flux (9 $m_{H2O}.yr^{-1}$ for mean flow conditions, 2.5 $m_{H2O}.yr^{-1}$ for low flow conditions), a length of 500 m for the sloping regolith layer and a circulation period of 10 years. In reality, as explained in chap. 3, both the water discharge and chemistry of granite springs vary largely along the slope and within the year. But it appears in most concentration diagrams that all measured spring data are spread along rather narrow, continuous scatters from low to high concentrations (Fig. 8).

It is not possible to take explicitly into account and simulate these measured space and time variations using the 1D KIRMAT code, which assumes a constant flux all along the modelled column. However, the sensitivity of the simulations to the interaction time could at least be

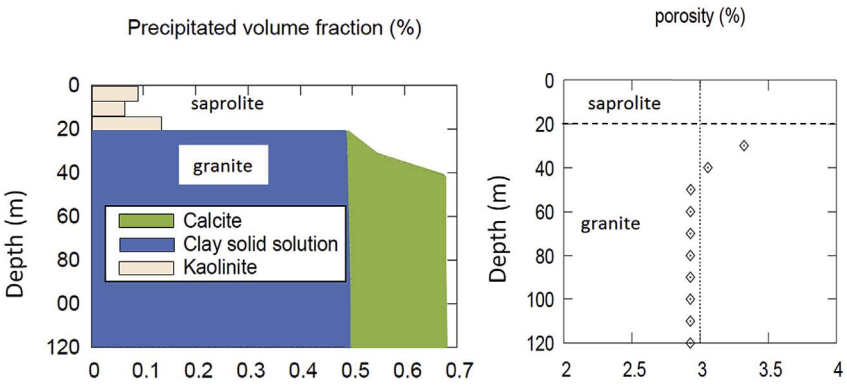

Fig. 6. Simulated final profiles in F-HUR granite after 10,000 years of weathering: (a) precipitated mineral volume (% volume) and the part of the different secondary phases; (b) porosity profile.

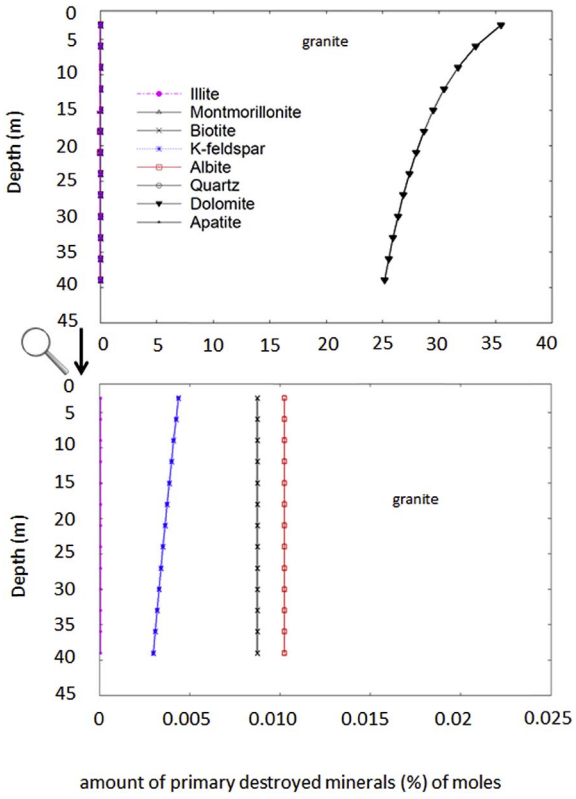

Fig. 7. Simulated final amounts (% of moles) of minerals destroyed along the F-HEI profile after 10,000 years of weathering in granite (for saprolite, see Fig. 5).

tested, using several combinations of values for its controlling factors: a larger range of input water flux (1.5, 2.5, 9 and 18 $m_{H2O}.yr^{-1}$) with a length of 500 m, 2 slope lengths (500 m, 1000 m) with a flux of 9 $m_{H2O}.yr^{-1}$. The smaller the flux for a given length, or the longer the length for a given flux, the longer the interaction time.

As illustrated for Mg and H_4SiO_4 on Fig. 9, all these combinations lead to simulated final concentration profiles, whose superposition defines a single main curve in concentration diagrams. In addition, the range of variation covered on this curve by a given combination tends to decrease when the imposed interaction time decreases. Mean flow (9 $m_{H2O}.yr^{-1}$) simulations cover most of the variation range of these main curves and fit reasonably well the measured concentration scatters of the granite spring waters in most cases (Fig. 8). These results on water chemistry only therefore provide some indirect validation of the hydrogeochemical simulations, despite the approximations made in the model.

For the 2.5 $m_{H2O}.year^{-1}$ flux along the 500 m profile, the simulated solution is supersaturated with respect to quartz and apatite. The simulated solution is undersaturated with respect to all other silicate minerals (albite, anorthite, biotite), except for K-feldspar, along the profile. Kaolinite is in equilibrium along the profile and solution is undersaturated with respect to calcite, regardless of the variations in the water flux. The precipitated clay is a smectite that is rich in exchangeable Ca and Mg but contains very little Fe and Na.

The precipitation dynamics of the clay solid-solution vary as a function of variations in the water flux. For the lowest flux (1.5 $m_{H2O}.yr^{-1}$), the clay solid-solution precipitates along most of the slope, from 150 m downwards; for a water flux of 2.5 $m_{H2O}.yr^{-1}$, the clay phase precipitates on the lower half of the slope, from 225 m downwards; for higher fluxes (9 $m_{H2O}.yr^{-1}$), the solution can become undersaturated with respect to clays throughout the 500 m-profile, but not on the whole 1000 m-profile, from 775 m downwards (show in Supplementary Fig. S1).

For very high flow rates, the supply of ions in the solution produced by the dissolution of silicate minerals is almost negligible due to the short water-rock interaction time. Since transport is the most important process, the composition of the input solution will control the chemical composition of the simulated water.

When the water flux decreases, the dissolution of silicate minerals becomes more and more significant because of longer interaction times. The resulting concentrations increase, differently for each element, and depend on the dissolution kinetics of the mineral containing the considered element. Finally, for low flow rates, the duration of the water-rock interaction may be sufficient for the aqueous solution to reach saturation with respect to the clay solid-solution. Aqueous silica is easily incorporated into the clay phases (including not only smectite-type solid-solution but also kaolinite). Then, the flux of silica precipitated by the solid solution becomes dominant, which explains the sudden reduction of the concentrations in the simulated water.

These results demonstrate that the variations in the composition of the spring waters can be interpreted in terms of different water-rock interaction durations: the spatial and temporal variations are explained by the same general scheme in which pathway length and water flux are the two parameters that determine the duration of this water-rock interaction.

5.4. Sensitivity analysis

All the previous simulations used key parameters (Eh, porosity, pCO_2), whose values are in fact affected by some uncertainty. Therefore, the sensitivity of the simulated results to the value of these parameters has also been tested by individually varying their values, taking as references these previous values and simulations. Some results of these tests are presented together with the reference curves in Fig. 10a for F-HUR borehole and in Fig. 10b for springs. As there is no difference concerning cations when using a redox potential Eh of 100 mV instead of the reference value of 250 mV, these simulations are not shown.

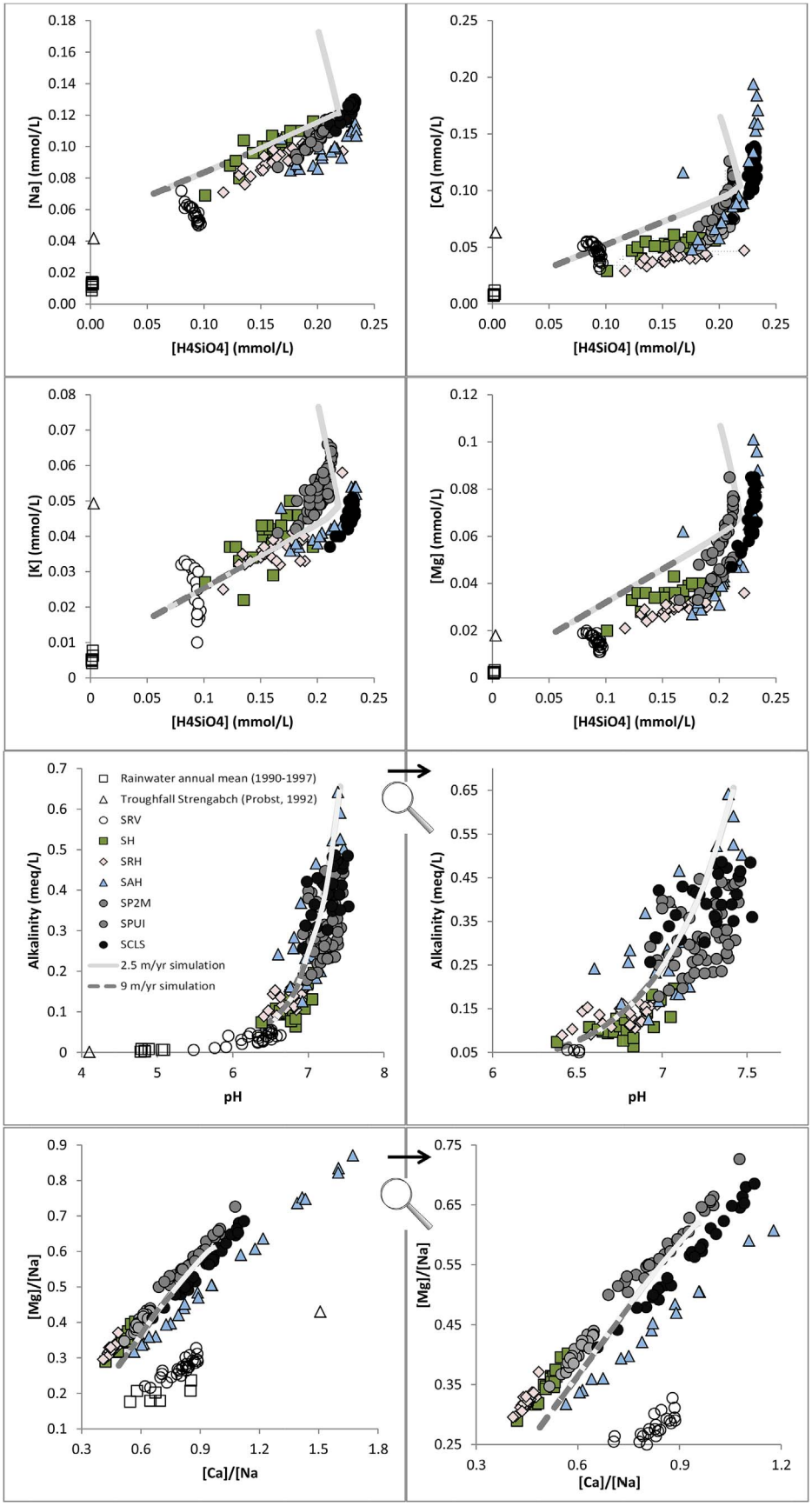

Fig. 8. Variations of simulated (KIRMAT) final water concentration along the sloping regolith layer after 10 years of weathering and comparison with measured granitic spring water samples. Simulated concentrations increase downslope. Simulation conditions: 2 input water fluxes: 9 $m_{H2O}.yr^{-1}$ (mean flow), $2.5m_{H2O}.yr^{-1}$ (low flow); 500 m slope length; calibrated regolith mineralogy.

Table 6
Calibrated mineralogical composition (%) and reactive surface areas *Sp* ($m^2.kg^{-1}_{H2O}$) of the regolith ("fresh" granite after 100,000 years of numerical weathering).

Minerals	Volume fraction (%)	Reactive surface area *Sp* ($m^2.kg^{-1}_{H2O}$)	Porosity (%)
Quartz	26.0	27.92	
Albite	14.4	15.75	
Anorthite	2.9	4.09	
Biotite	20.5	22.33	
K-Feldspar	28.1	3.01	
Apatite	1.3	1.23	
Amphibole	1.9	2.13	
Kaolinite	4.6	0.01	
Hematite	0.1	0.001	
Total	100	76.48	5.38

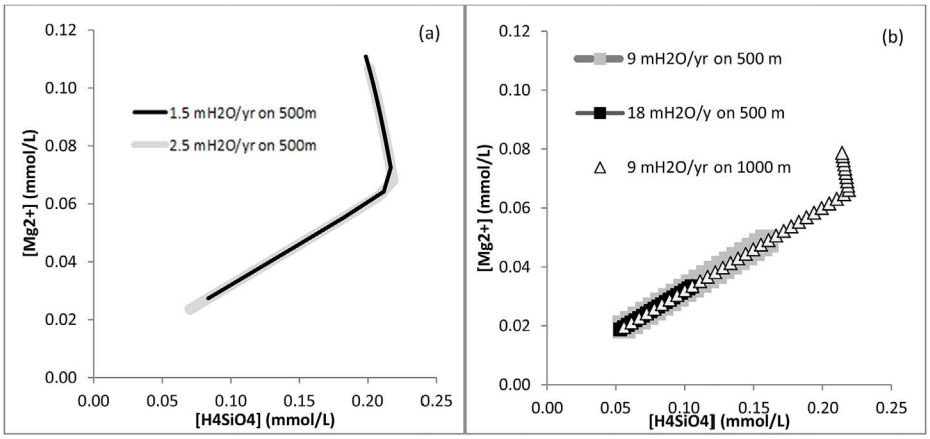

Fig. 9. Variations of simulated final Mg and H_4SiO_4 concentrations along the sloping regolith layer after 10 years of weathering for: (a) 4 input water fluxes; (b) 2 slope lengths (top: 0 m, base: 500 m or 1000 m).

For borehole waters (Fig. 10a), the granite porosity, whose reference value is 3%, seems not to be a sensitive parameter. The Na vs H_4SiO_4 curve simulated using a higher granite porosity of 6% is close to the reference one, even though it does not reach the same higher levels of both concentrations. As the reactive surfaces decrease with higher porosity, reactions do not go so far. The most sensitive parameter is pCO_2, whose reference value is 10^{-3} atm. For a lower value of 10^{-4} atm, the Na vs H_4SiO_4 curve is slightly shifted towards higher H_4SiO_4 concentrations. For a higher value of 2.10^{-3} atm, the curve is much more shifted towards higher Na concentrations, but it still correspond in its upper part to the upper envelop of the measured point scatter. For spring waters, the only slightly sensitive parameter seems to be the regolith porosity, whose reference value is 5.38%. For a porosity of 10%, the Na vs H_4SiO_4 curve overlaps the lower part of reference curve but is shorter, as reactions do not go so far (Fig. 10b).

The published dissolution rate determined in the laboratory for biotite (Table 5) was also tested for comparison with the adjusted reduced reference value. For both borehole and spring waters, it leads to much too high, unrealistic K concentrations (Fig. 10). As already suggested in the literature, this case study confirms that it may be necessary to use dissolution rates values lower than that estimated in the laboratory.

This limited sensitivity analysis, which concerns key parameters controlling simulations, shows that the model and parametrization used here give rather robust results, leading to the same simulated geochemical behaviors for parameter values remaining within their uncertainty ranges.

6. Conclusions

The results of this study highlight the applicability of coupled hydrogeochemical modeling approaches to the origins of variations in water chemical compositions at the catchment scale. And the rather good simulation results obtained for waters give some confidence in the results obtained for the much less constrained rock composition and weathering.

The application of these approaches to the Ringelbach catchment allows us to not only constrain the very contrasting geochemical characteristics of the borehole waters compared to the spring waters but also to understand the chemical diversity of waters within each of these hydrological contexts. These differences are related to the different types of pathways of the water supplying boreholes and springs within the bedrock, each of which these pathways crosses different types of waters but is also marked by different hydrological characteristics: waters supplying the springs feature a near surface and relatively fast flow (about 9 $m_{H2O}.yr^{-1}$), which is more or less parallel to the slope, whereas the borehole waters feature a more vertical and slower flow (0.5–0.1 $m_{H2O}.yr^{-1}$).

For borehole waters, this model allows us to account for the difference between vertical flows in a regular porous medium (F-HUR) and in a porous medium crossed by a sub-vertical fracture (F-HEI). Both of these hydrodynamical contexts, which are inherited from the regional geological history, explain the chemical contrasts between the F-HUR and F-HEI waters, especially by influencing the reactive surface areas of minerals involved in the water-rock interactions. Furthermore, in the F-HUR case, the feedback effect on porosity modeled by the KIRMAT code

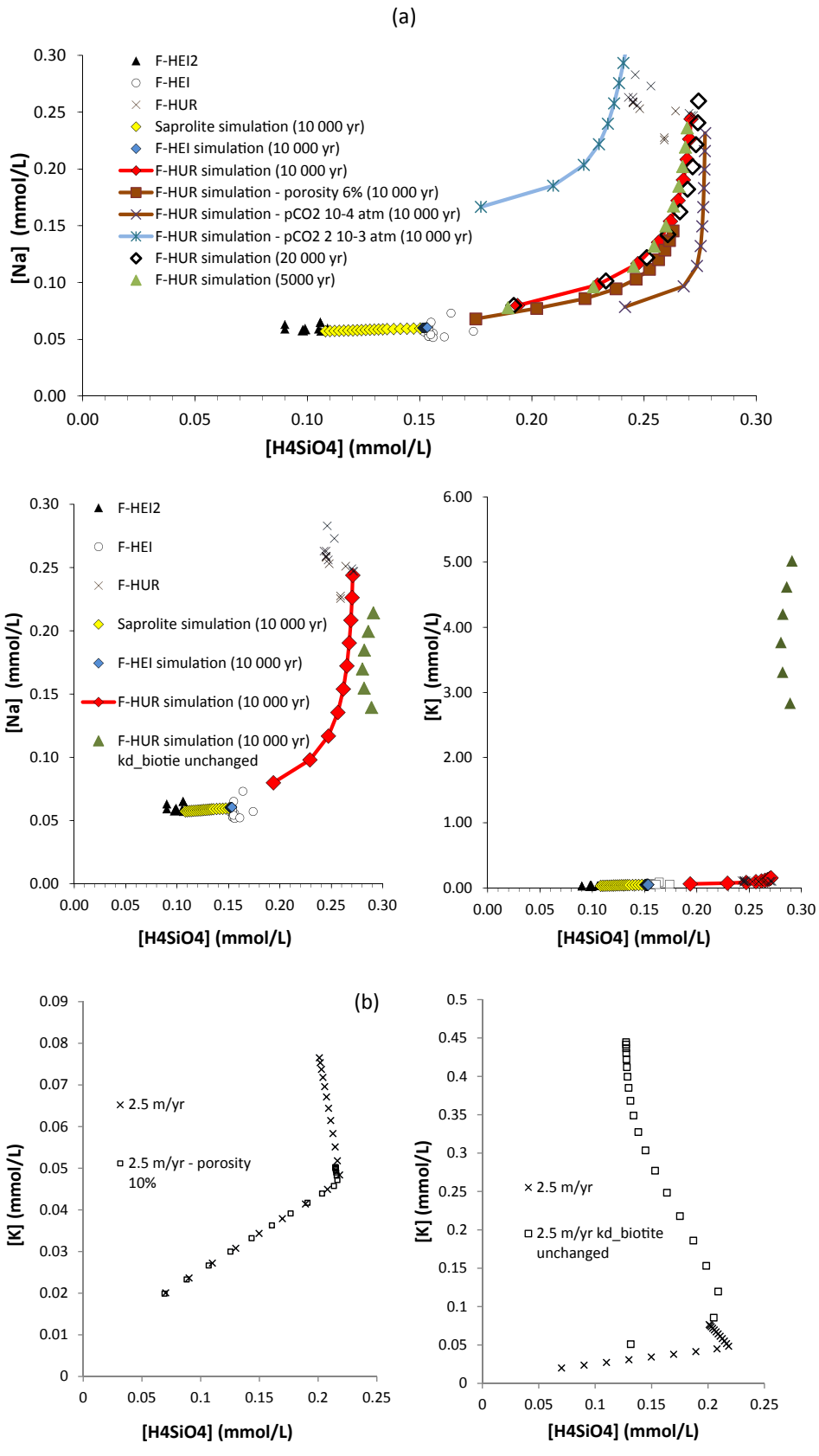

Fig. 10. Sensitivity of the simulations to the value of some key parameters: (a) for F-HUR borehole waters (reference simulation parameters: duration 10,000 yr, porosity 3%, pCO_2 10^{-3} atm; tested parameters: 20,000 and 5000 yr, porosity 6%, pCO_2 2.10^{-3} and 10^{-4} atm); (b) for spring waters (reference simulation porosity 5.38%; tested porosity 10%). In both cases, the unchanged biotite dissolution rate is the laboratory value (Log kd = -5.247 mol m^{-2}. yr^{-1}), for F-HUR borehole waters this value is divided by 50, for spring waters this value is divided by 10.

could also explain the formation of the "weathering profile", as observed along the borehole, by creating a disconnect between its effects on porosity of the top of the profile and the fresh bedrock.

For spring waters, this model allows us to constrain the nature of rock of the pathway: it is neither saprolite nor fresh granite, but instead a weathered granite with a weathering age of several tens of thousands of years. Spatial and temporal variations in the chemical compositions of spring water can be explained as the result of the same circulation pattern for which the water-rock interaction time is determined by the length of the pathway and the water velocity. When this water-rock interaction time is sufficient, the precipitation of clay phases plays a major role in determining the chemical composition of the water.

Despite the one-dimensional approach and the crude approximations made on the system geometry and complexity, the uncertainty on water fluxes, rock mineralogy and kinetic data, this study shows that the coupled hydrogeochemical modeling is a powerful tool for a better understanding of weathering processes and the coupling that exists between water circulation dynamics and water-rock interactions.

Acknowledgments

This study was funded by the French "Programme National de Recherche en Hydrologie" (ECCO/PNRH 2004-07), with co-funding provided by the Programme REALISE (CPER État-Région Alsace 2005) for the borehole drilling.

All geochemical analyses were performed at the Laboratoire d'Hydrologie et de Géochimie de Strasbourg (LHyGeS/EOST). We warmly thank D. Million and S. Gangloff for these analyses.

Appendix E. Supplementary data

Supplementary data related to this article can be found at http://dx.doi.org/10.1016/j.apgeochem.2017.10.005.

Appendix A. Mineral phases identified by X-ray diffraction on core samples from F-HUR and F-HEI boreholes: (1) in the total rock; (2) in the clay size fraction (< 2 µm). The star number (from 0 to 4) gives a qualitative indication of increasing proportion.

(1)

Core sample	Upper depth (m)	Lower depth (m)	Sample type (Wyns, 2012)	Quartz	Feldspath K	Albite	Calcite	Dolomite	Apatite	Hematite
F-HUR 17	28.23	28.30	saprolite	****	**					*
F-HUR 21	35.71	35.77	saprolite	****	**			*		*
F-HUR 24	43.76	43.85	saprolitesaprolite	****	**			*	*	
F-HUR 26	50.92	51.02	fissured porphyritic granite	****	*	**		*	*	
F-HUR 29	63.17	63.25	fissured porphyritic granite	****	*	*			*	
F-HUR 33	77.34	77.44	fissured porphyritic granite	****	*	*	*	*		*
F-HUR 36	89.92	90.00	fissured porphyritic granite	****	*	*		*	*	
F-HUR-38	93.96	94.06	fault breccia	****	*					*
F-HUR 41	105.20	105.30	fissured porphyritic granite	***	**	**			*	
F-HUR 46	122.95	123.09	fissured porphyritic granite	****	*	*		*		
F-HUR 50	139.28	139.44	geode in fine granite	***	*	*	***	*		
F-HUR 53	148.00	148.06	fine granite	****	*	**		*		
F-HEI 01	101.95	102.02	very weathered fissured porphyritic granite	****	**		*	*		
F-HEI 05	116.95	117.05	weathered fissured porphyritic granite	****	**					*
F-HEI 07	127.98	128.04	weathered fissured porphyritic granite	****	**			*		*
F-HEI 12	146.20	146.30	weathered fissured porphyritic granite	****	**			*		*

(2)

Core sample	Upper depth (m)	Lower depth (m)	Sample type (Wyns, 2012)	Illite	Smectite	Ill/Sm	Kaolinite	Vermiculite	Chlorite	Quartz	Feldspath	Calcite
F-HUR 17	28.23	28.30	saprolite	****		*	**					
F-HUR 21	35.71	35.77	saprolite	***	*	*	*					
F-HUR 24	43.76	43.85	saprolite	**	**	**	*					
F-HUR 26	50.92	51.02	fissured porphyritic granite	****	**	**						
F-HUR 29	63.17	63.25	fissured porphyritic granite	****				*		*	*	
F-HUR 33	77.34	77.44	fissured porphyritic granite	****	**		*	*				
F-HUR 36	89.92	90.00	fissured porphyritic granite	**	****	*						
F-HUR-38	93.96	94.06	fault breccia	****		**						
F-HUR 41	105.20	105.30	fissured porphyritic granite	****	*							
F-HUR 46	122.95	123.09	fissured porphyritic granite	****	*		*		*			
F-HUR 50	139.28	139.44	geode in fine granite	**	**					*	*	*
F-HUR 53	148.00	148.06	fine granite	**	**	*			*	*	*	
F-HEI 01	101.95	102.02	very weathered fissured porphyritic granite	**	****	*						
F-HEI 05	116.95	117.05	weathered fissured porphyritic granite	****		*						
F-HEI 07	127.98	128.04	weathered fissured porphyritic granite	****		**	*					
F-HEI 12	146.20	146.30	weathered fissured porphyritic granite	****		*	**					

Appendix B. (1) Trace elements measured by ICP-AES for borehole waters in F-HEI2, F-HEI and FHUR. Concentrations below detection limit are noticed with "-", not measured with "n.m."; (2) Major element concentrations (detection limit: 0.001 mmol.L-1) of: (a) the F-HEI2, F-HEI and F-HUR borehole waters; and (b) spring waters (1st and 2nd lines: maximum and minimum of discharge or conductivity; 3rd line: average. Extracted from Schaffhauser et al. (2014)).

(1)

F-HUR

Water sample	Sampling depth (m)	Al (µmol.L^{-1})	Fe (µmol.L^{-1})	Mn (µmol.L^{-1})	P (µmol.L^{-1})	H_4SiO_4 (µmol.L^{-1})
detection limit (µmol.L^{-1})		**0.37**	**0.04**	**0.02**	**0.97**	**0.36**
14/10/2008	63	0.37	–	0.036	–	279.85
14/10/2008	75	–	–	0.036	–	277.72
14/10/2008	90	0.74	–	0.036	–	279.85
14/10/2008	120	0.74	–	0.018	–	252.08
14/10/2008	140	0.37	–	0.055	–	252.08
	Sampling depth (m)	Al (µmol.L^{-1})	Fe (µmol.L^{-1})	Mn (µmol.L^{-1})	P (µmol.L^{-1})	H_4SiO_4 (µmol.L^{-1})
detection limit (µmol.L^{-1})		**0.07**	**0.01**	**0.002**	**0.13**	**0.10**
07/07/2009	61	0.19	–	0.016	0.23	288.10
07/07/2009	75	–	–	0.019	0.45	288.90
07/07/2009	90	0.11	–	0.015	0.45	290.10
07/07/2009	120	0.19	–	0.007	0.29	274.20
07/07/2009	140	0.15	–	0.013	0.36	265.80

13/10/2010	65	–	–	0.046	0.29	279.20
13/10/2010	75	0.07	–	0.026	0.45	278.00
13/10/2010	90	–	–	0.021	0.32	284.00
13/10/2010	105	n.m.	n.m.	n.m.	n.m.	n.m.
13/10/2010	120	0.22	–	0.012	0.45	265.70
13/10/2010	140	0.30	–	0.005	0.55	266.30

F-HEI-2

	Sampling depth (m)	Al (µmol.L^{-1})	Fe (µmol.L^{-1})	Mn (µmol.L^{-1})	P (µmol.L^{-1})	H_4SiO_4 (µmol.L^{-1})
detection limit (µmol.L^{-1})		**0.07**	**0.01**	**0.002**	**0.10**	**0.10**
10/06/2008	47	n.m.	n.m.	n.m.	n.m.	n.m.
10/06/2008	55	n.m.	n.m.	n.m.	n.m.	n.m.
14/10/2008	48	n.m.	n.m.	n.m.	n.m.	n.m.
14/10/2008	55	n.m.	n.m.	n.m.	n.m.	n.m.
07/07/2009	48	0.11	–	0.14	–	111.10
07/07/2009	55	0.11	–	0.13	–	111.70
12/10/2010	50	0.19	–	0.14	–	115.30
12/10/2010	55	0.11	–	0.12	–	113.80

F-HEI

Water sample	Sampling date	Sampling depth (m)	Al (µmol.L^{-1})	Fe (µmol.L^{-1})	Mn (µmol.L^{-1})	P (µmol.L^{-1})	H4SiO4 (µmol.L-1)
detection limit (µmol.L^{-1})			**0.74**	**0.072**	**0.0073**	**2.58**	**0.36**
F-HEI during pumping at depth [−]	14/05/2008	[100]	0.74	–	0.0419	–	164.49
F-HEI during pumping at depth [−]	14/05/2008	[138]	1.48	0.197	0.1675	3.23	169.12
F-HEI after pumping	14/05/2008	140	1.11	0.125	0.4023	–	222.17
F-HEI	10/06/2008	140	n.m.	n.m.	n.m.	n.m.	n.m.
F-HEI	14/10/2008	140	n.m.	n.m.	n.m.	n.m.	n.m.

Water sample	Sampling date	Sampling depth (m)	Al (µmol.L^{-1})	Fe (µmol.L^{-1})	Mn (µmol.L^{-1})	P (µmol.L^{-1})	H4SiO4 (µmol.L-1)
detection limit (µmol.L^{-1})			**0.07**	**0.01**	**0.002**	**0.1**	**0.1**
F-HEI	07/07/2009	140	0.81	0.16	–	2.3	167.1
F-HEI 1/2	11/10/2010	140	–	–	0.029	2.5	161.6
F-HEI 2/2	11/10/2010	140	0.37	–	0.371	2.4	166.7
F-HEI during pumping at depth [−]	13/10/2010	[140]	0.11	–	–	3.2	164.6

(2-a)

Sampling date	depth (meters)	Conductivity 20 °C (µS/cm)	pH	Alkalinity (meq/L)	[$NH4^+$] (mmol/L)	[Na^+] (mmol/L)	[K^+] (mmol/L)	[Mg^{2+}] (mmol/L)	[Ca^{2+}] (mmol/L)	[Cl^-] (mmol/L)	[NO_3^-] (mmol/L)	[SO_4^{2-}] (mmol/L)	[PO_4^{3-}] (mmol/L)	[H_4SiO_4] (mmol/L)	NPOC (mg/kg C)
F-HEI *(7°07′00.196″ E/48°05′04.038″ N)*															
average	96.5	80.97	7.653	0.800	0.011	0.053	0.050	0.117	0.265	0.040	0.026	0.010	0.007	0.155	1.000
14/05/2008	100	87.00	7.570	0.827	< 0.001	0.054	0.054	0.119	0.292	0.043	0.029	0.010	0.003	0.155	0.210
14/05/2008	138	91.50	7.650	0.877	< 0.001	0.052	0.053	0.12	0.318	0.042	0.028	0.012	0.003	0.161	0.140
average	140	93.45	7.633	0.932	< 0.001	0.061	0.064	0.117	0.331	0.043	0.028	0.016	0.006	0.159	0.267
F-HEI2 *(7°07′00.491″ E/48°05′04.067″ N)*															
10/6/2008	47	26.9	6.700	0.034	< 0.001	0.059	0.031	0.015	0.046	0.058	0.018	0.05	0.001	0.099	0.550
average	47	26.9	6.700	0.034	< 0.001	0.059	0.031	0.015	0.046	0.058	0.018	0.05	< 0.001	0.099	0.550
12/10/2010	50	26	6.300	0.06	< 0.001	0.058	0.034	0.02	0.043	0.054	0.019	0.039	< 0.001	0.109	< 0.560
average	48	26.6	6.567	0.0427	< 0.001	0.059	0.032	0.0177	0.045	0.057	0.018	0.046	< 0.001	0.102	0.550
F-HUR *(7°07′25.180″ E/48°04′54.700″ N)*															
7/7/2009	61	221.60	8.010	2.500	< 0.001	0.249	0.104	0.614	0.563	0.087	0.056	0.016	< 0.001	0.270	0.230
14/10/2008	63	208.90	8.200	2.360	< 0.001	0.302	0.112	0.560	0.540	0.096	0.046	0.024	< 0.001	0.256	0.400
13/10/2010	65	208.80	8.350	2.360	< 0.001	0.228	0.095	0.580	0.505	0.072	0.045	0.026	< 0.001	0.259	< 0.560
average	75	213.80	8.203	2.413	< 0.001	0.243	0.101	0.580	0.538	0.082	0.047	0.021	< 0.001	0.262	0.220
average	90	217.13	8.230	2.507	< 0.001	0.256	0.100	0.618	0.542	0.083	0.045	0.017	0.008	0.264	0.220
average	120	242.73	8.313	2.860	< 0.001	0.284	0.102	0.723	0.603	0.083	0.036	0.031	0.007	0.242	0.290

(2-b)

sampling date	Discharge (L/s)	Conductivity 20 °C (µS/cm)	pH	Alkalinity (meq/L)	[$NH4^+$] (mmol/L)	[Na^+] (mmol/L)	[K^+] (mmol/L)	[Mg^{2+}] (mmol/L)	[Ca^{2+}] (mmol/L)	[Cl^-] (mmol/L)	[NO_3^-] (mmol/L)	[SO_4^{2-}] (mmol/L)	[PO_4^{3-}] (mmol/L)	[H_4SiO_4] (mmol/L)	NPOC (mg/kg C)
Spring SRV *(7°07′02.867″ E/48°04′57.986″ N)*															
8/3/2002	0.88	27.4	5.91	0.013	< 0.001	0.061	0.032	0.019	0.054	0.063	0.016	0.071	< 0.001	0.083	0.81
18/12/2003	0.0083	24	6.51	0.055	< 0.001	0.058	0.022	0.019	0.051	0.088	< 0.001	0.031	< 0.001	0.092	3.06
average	0.17263	22.58214	6.314	0.03661	< 0.001	0.05664	0.0251	0.015357	0.04518	0.05693	0.01127	0.04875	< 0.001	0.09161	0.98714
Spring SH *(7°07′15.787″ E/48°04′49.109″ N)*															
24/01/2005		28.2	6.68	0.094	< 0.001	0.096	0.04	0.035	0.05	0.06	0.101	0.021	< 0.001	0.152	0.97
25/10/2005		36.5	7.05	0.131	< 0.001	0.11	0.05	0.04	0.059	0.068	0.115	0.021	< 0.001	0.176	0.73
average		31.57	6.788	0.1167	< 0.001	0.0986	0.03845	0.03505	0.05115	0.056	0.0899	0.0206	< 0.001	0.154	0.969

Spring SRH *(7°07′11.622″ E/48°04′49.361″ N)*														
24/02/2005		26.1	6.81	0.114	< 0.001	0.087	0.036	0.028	0.04	0.042	0.06	0.021	< 0.001	0.151	1.04
10/3/2006		20	6.58	0.091	< 0.001	0.071	0.025	0.021	0.029	0.026	0.041	0.015	0.001	0.117	1.47
average		26.7259	6.774444	0.132	< 0.001	0.09115	0.03633	0.0294	0.041037	0.03874	0.05081	0.02078	0.0011	0.1632	0.9663
Spring SAH *(7°07′06.571″ E/48°04′51.283″ N)*														
5/10/2004		67.5	7.39	0.642	< 0.001	0.116	0.054	0.101	0.194	0.039	0.011	0.037	< 0.001	0.23	0.68
10/3/2006		27.8	6.92	0.126	< 0.001	0.085	0.036	0.027	0.048	0.049	0.032	0.029	0.001	0.176	1.35
average		43.2696	7.096957	0.33	< 0.001	0.09943	0.0443	0.0552	0.104	0.03922	0.02135	0.03252	< 0.001	0.2093	0.71261
Spring SP2M *(7°07′05.448″ E/48°04′47.413″ N)*														
30/08/2005	0.1083	37.4	7.43	0.307	< 0.001	0.113	0.051	0.049	0.073	0.027	0.031	0.019	< 0.001	0.21	0.57
10/3/2006	2.0248	29.4	6.98	0.178	< 0.001	0.087	0.041	0.033	0.05	0.028	0.045	0.018	0.001	0.165	1.11
average	0.36787	34.46296	7.192	0.26159	< 0.001	0.10637	0.0486	0.042852	0.06374	0.02815	0.03359	0.01833	0.001	0.19789	0.6537
Spring SPUI *(7°07′00.995″ E/48°04′44.929″ N)*														
18/12/2003	0.0525	56.9	7.35	0.476	< 0.001	0.117	0.066	0.085	0.126	0.029	0.023	0.03	< 0.001	0.209	0.8
24/01/2005	0.97	35.9	7.24	0.308	< 0.001	0.105	0.053	0.056	0.081	0.035	0.024	0.025	< 0.001	0.2	0.64
average	0.64693	44.575	7.264	0.36814	< 0.001	0.10918	0.058	0.063964	0.09518	0.03136	0.02375	0.02579	< 0.001	0.20443	0.61929
Spring SCLS *(7°06′52.366″ E/48°04′38.323″ N)*														
8/3/2002		36.6	6.93	0.257	< 0.001	0.114	0.037	0.047	0.075	0.032	0.027	0.032	0.001	0.211	0.6
18/12/2003		58.5	7.34	0.482	< 0.001	0.125	0.05	0.085	0.137	0.032	0.018	0.032	< 0.001	0.228	0.53
average		49.2786	7.270714	0.399	< 0.001	0.12364	0.04596	0.0695	0.114857	0.03629	0.03243	0.02971	< 0.001	0.228	0.56071

Appendix C. Porosities and permeabilities measured on core samples from F-HUR and F-HEI boreholes. Sources: BRGM (Baltassat, 2017), IPGS (Schaffhauser et al., 2014), LGHF (Haceb, 2006). Adapted from Schaffhauser (2013).

Borehole	mean core sample depth (m)	lithologic type	Porosity (%)	average permeability (m^2)
	7.07	fine sandstone	22.2	
	13.47	medium sandstone	11.0	
F-HUR	20.85	coarse sandstone	11.2	
	24.84		16.06	1.22E-14
	27.24	sandstone	17.32	
	27.33		17.75	
	27.85	coarse sandstone	16.6	
	29.80	flaky saprolite	16.5	
F-HUR 17	**28.27**	saprolite		
F-HUR 21	**35.75**	saprolite		
	37.85	flaky saprolite	10.6	
F-HUR 24	**43.81**	saprolite		
	49.84	fine granite	1.40	9.12E-19
	50.11	fine granite	3.66	1.25E-16
F-HUR 26	**50.97**	fissured porphyritic granite		
	52.55	not healthy fissured granite	1.8	
	61.07	fissured porphyritic granite	2.27	6.72E-18
	61.18	fissured porphyritic granite	5.47	2.85E-16
	61.28	fissured porphyritic granite	2.32	1.16E-17
	61.53	red healthy granite	2.19	
F-HUR 29	**63.21**	fissured porphyritic granite		
F-HUR 33	**77.39**	fissured porphyritic granite		
	78.76	gray porphyritic granite	0.67	3.82E-19
	78.82	gray porphyritic granite	0.79	1.87E-18
	79.13	gray porphyritic granite	0.61	9.60E-19
	79.91	healthy granite	1.30	
	80.07	healthy granite	1.26	
	82.74	red weakly weathered granite	2.76	
F-HUR 36	**89.96**	fissured porphyritic granite		
F-HUR 38	**94.01**	fault breache		
	97.30	red fractured granite	6.70	
	98.58	healthy porphyritic granite	1.25	3.19E-19
F-HUR 41	**105.25**	fissured porphyritic granite		
	111.08	weathered granite	3.21	
	111.20	weathered granite	3.56	
	113.61	healthy porphyritic granite	1.30	3.65E-18
	116.54	fresh fissured granite	0.7	
F-HUR 46	**123.02**	fissured porphyritic granite		
	130.11	granite porphyritic healthy	0.52	6.95E-23
	131.56	healthy granite	1.63	
F-HUR 50	**139.35**	porphyritic granite		
	146.41	weathered granite	6.09	
	146.53	weathered granite	2.42	
F-HUR 53	**148.03**	fine granite		
	148.33	fine granite	1.64	4.26E-18
F-HEI				
F-HEI	101.99	weathered granite		
F-HEI	102.17	weathered granite		
F-HEI	117.81	red fractured granite	7.43	
F-HEI	140.23	red fractured granite	4.49	
F-HEI	122.86		11.1	

Appendix D. Simplified hydrogeological model used to estimate the main groundwater fluxes within the structured bedrock. (1)

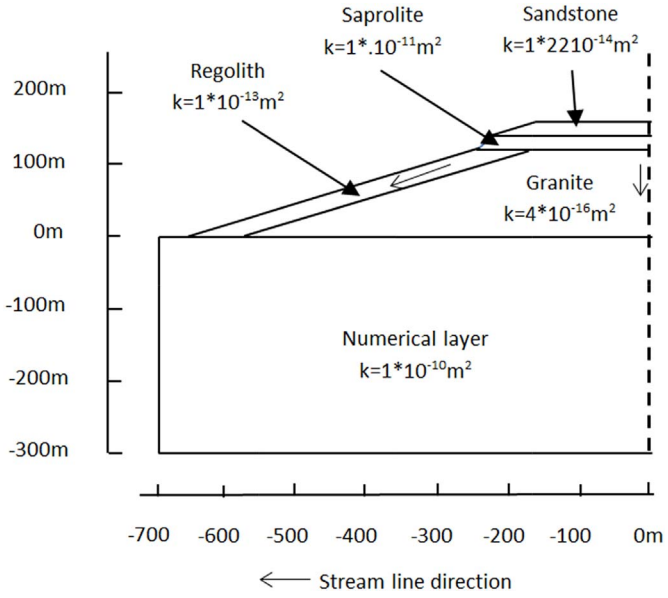

The 2D hydrogeological model corresponds to the vertical section of the bedrock along the fall line of the Hurlin slope passing through F-HUR borehole. It is a rough approximation because of poorly known bedrock geometry and properties. The upper limit follows the actual slope topography. Four layers are implemented: 3 horizontal layers, sandstone (20 m thick), saprolite (20 m thick), fissured granite, and a superficial sloping regolith horizon (including the soil) along the slope (calibrated thickness). Based on the available permeability measurements on core samples (Appendix C), the sandstone permeability k is fixed at 1.22×10^{-14} m^2. Granite samples have highly variable permeability, ranging from 6.95×10^{-23} to 2.85×10^{-16} m^2. Since granite is fractured, the chosen value (4×10^{-16} m^2) has been selected a little bigger than the highest measured value (2.85×10^{-16} m^2). The saprolite permeability is fixed at 8×10^{-12} m^2, a value within the range found in the literature (Mulla and McBratney, 2000). To obtain a realistic simulated water table, calibrated values of permeability (2×10^{-14} m^2) and thickness (22 m) are used for the regolith layer. While much more permeable, the shallow soil layer at the top of the regolith is not explicitly taken into account in this simplified model.

As no piezometric data are available except in boreholes, the water table within the regolith is assumed to follow the slope topography. An arbitrary value is set for the unknown thickness of the fissured granite, with a null flux limit at the bottom. For the lateral limits, a symmetry axis is assumed on one side. On the other side, a constant head of 800 m, equal to the topographic level, is set at the base of the slope. The difference (0.65 $m_{H2O}.yr^{-1}$) between mean annual precipitation (1.25 $m_{H2O}.yr^{-1}$) and potential evapotranspiration (0.6 $m_{H2O}.yr^{-1}$) is used as a crude estimation of the groundwater recharge flux through the soil bottom.

Simulations are performed at steady-state, by solving Darcy's law. The following simulated fluxes have then been used as input water fluxes in the 1D hydrogeochemical modeling (Fig. 2). For the saprolite (0.5 $m_{H2O}.yr^{-1}$) and the “fresh” F-HUR granite (0.1 $m_{H2O}.yr^{-1}$), they are the vertical fluxes simulated on the symmetry axis at the top of the layer (fluxes per horizontal surface unit). For the more weathered and fractured F-HEI granite, it is assumed to be 0.5 $m_{H2O}.yr^{-1}$ as for the saprolite.

For the sloping regolith layer, the average 9 $m_{H2O}.yr^{-1}$ of the downslope flux simulated along its mid-depth line has been used as input flux in mean flow conditions. If the regolith thickness was chosen to be smaller, this flux would have been more important. A flux of 2.5 $m_{H2O}.yr^{-1}$ has also been used as representative of low flow conditions, as suggested by a previous study (Schaffhauser et al., 2014) using a Uranium modeling approach to estimate the springs recharge. Discussion on flux variability will be led in the paragraph 5.3.2.

References

Ambroise, B., 1995. Topography and the water cycle in a temperate middle mountain environment: the need for interdisciplinary experiments. Agric. For. Meteorology 73, 217–235.

Ambroise, B., 2016. Variable water-saturated areas and streamflow generation in the small Ringelbach catchment (Vosges Mountains, France): the master recession curve as an equilibrium curve for interactions between atmosphere, surface and ground waters. Special Issue “Keith Beven Tribute”. Hydrol. Process. 30 (20), 3560–3577. http://dx.doi.org/10.1002/hyp.10947.

Ambroise, B., Freer, J., Beven, K., 1996. Application of a generalized TOPMODEL to the small Ringelbach catchment, Vosges, France. Water Resour. Res. 32, 2147–2159.

Ambroise, B., Viville, D., 1986. Spatial variability of textural and hydrodynamical properties in a soil unit of the Ringelbach study catchment, Vosges (France). Z. für Geomorphol. Suppl. Band. 58, 21–34.

Aubert, D., Stille, P., Probst, A., 2001. REE fractionation during granite weathering and removal by waters and suspended loads: Sr and Nd isotopic evidence. Geochimica Cosmochimica Acta 65 (3), 387–406.

Baltassat, J.M., 2017. Réinterprétation des investigations géophysiques du bassin du Ringelbach avec les données de forages et les mesures en laboratoire. Rapport final. BRGM/RP-66694-FR, 167 pp., 33 fig., 15 tabl., 13 ann.

Baltassat, J.M., Legchenko, A., Ambroise, B., Mathieu, F., Lachassagne, P., Wyns, R., Mercier, J.L., Schott, J.J., 2005. Magnetic resonance sounding (MRS) and resistivity characterisation of a mountain hard rock aquifer: the Ringelbach Catchment, Vosges Massif, France. Near Surf. Geophys. 3, 267–274.

Banwart, S., Bernasconi, S.M., Bloem, J., Blum, W., Brandao, M., Brantley, S., Zhang, B., 2011. Soil processes and functions in critical zone observatories: hypotheses and experimental design. Vadose Zone J. 10, 974–987.

Bertrand, C., Fritz, B., Sureau, J.F., 1994. Hydrothermal experiments and thermo-kinetic modelling of water-sandstone interactions. Chem. Geol. 116, 189–202.

Blum, A.E., Stillings, L.L., 1995. Feldspar dissolution kinetics. Rev. Mineralogy Geochem. 31, 291–351.

Bouma, T.J., Nielsen, K.L., Eissenstat, D.M., Lynch, J.P., 1997. Estimating respiration of roots in soil: interactions with soil CO2, soil temperature and soil water content. Plant Soil 195 (2), 221–232.

Brantley, S.L., Blai, A.C., Cremeens, D.L., Macinnis, I., Darmody, R.G., 1993. Natural etching rates of feldspar and hornblende. Aquat. Sci. 55 (4), 262–272.

Brantley, S.L., Goldhaber, M.B., Ragnarsdottir, K.V., 2007. Crossing disciplines and scales to understand the critical zone. Elements 3 (5), 307–314.

Bray, A.W., Oelkers, E.H., Bonneville, S., Wolff-Boenisch, D., Potts, N.J., Fones, G., Benning, L.G., 2015. The effect of pH, grain size, and organic ligands on biotite weathering rates. Geochem. Cosmochim. Acta 164, 127–145.
Chabaux, F., Viville, D., Lucas, Y., Ackerer, J., Ranchoux, C., Bosia, C., Pierret, M.C., Labasque, T., Aquilina, L., Wyns, R., Lerouge, C., Dezaye, C., Négrel, P., 2017. Geochemical tracing and modeling of surface and deep water–rock interactions in elementary granitic watersheds (Strengbach and Ringelbach CZOs, France). Acta Geochim. 1–4.
Dove, P.M., 1994. The dissolution kinetics of quartz in sodium chloride solutions at 25 degrees to 300 degrees C. Am. J. Sci. 294, 665–712.
Duplay, J., Semhi, K., Errais, E., Imfeld, G., Babcsanyi, I., Perrone, T., 2014. Copper, zinc, lead and cadmium bioavailability and retention in vineyard soils (Rouffach, France): the impact of cultural practices. Geoderma 230, 318–328.
Fritz, B., 1975. Étude thermodynamique et simulation des réactions entre minéraux et solutions, application à la géochimie des altérations et des eaux continentales. Sciences Géologiques, Mémoire 41. Université Louis Pasteur, Strasbourg 152pp.
Fritz, B., 1981. Étude thermodynamique et modélisation des réactions hydrothermales et diagénétiques. Sciences Géologiques, Mémoire 65. Université Louis Pasteur, Strasbourg Ed 197pp.
Fritz, B., 1985. Multicomponent solid solutions for clay minerals and computer modeling of weathering processes. In: Drever, J. (Ed.), The Chemistry of Weathering. Springer, Netherlands, pp. 19–34.
Fritz, B., Tardy, Y., 1976. Séquencede minéraux secondaires dans l'altération des granites et roches basiques: modèles thermodynamiques. Bull. Société Géologique Fr. 18, 7–12.
Gagny, C., 1968. Petrogenèse du granite des crêtes. Université de Nantes Ph.D., 546 pp.
Ganor, J., Lu, P., Zheng, Z., Zhu, C., 2007. Bridging the gap between laboratory measurements and field estimations of silicate weathering using simple calculations. Environ. Geol. 53, 599–610.
Ganor, J., Mogollón, J.L., Lasaga, A.C., 1995. The effect of pH on kaolinite dissolution rates and on activation energy. Geochimica Cosmochimica Acta 59, 1037–1052.
Garrels, R.M., Christ, C.L., 1967. Equilibres des minéraux et de leurs solutions aqueuses. Gauthier-Villars.
Gérard, F., Clément, A., Fritz, B., Crovisier, J.L., 1996. Introduction des phénomènes de transport dans le modèle thermo-cinétique KINDIS : le modèle KIRMAT. Comptes Rendus de l'Académie des Sciences, Paris, pp. 377–384 t. 322, Série IIa.
Gérard, F., Clément, A., Fritz, B., 1998a. Numerical validation of an Eulerian hydrochemical code using a 1-D multisolute mass transport system involving heterogeneous kinetically-controled reactions. J. Contam. Hydrology 30 (3–4), 199–214.
Gérard, F., Fritz, B., Clément, A., Crovisier, J.-L., 1998b. General implications of aluminium speciation-dependent kinetic dissolution rate law in water–rock modelling. Chem. Geol. 151, 247–258.
Goddéris, Y., François, L.M., Probst, A., Schott, J., Moncoulon, D., Labat, D., Viville, D., 2006. Modelling weathering processes at the catchment scale: the WITCH numerical model. Geochimica Cosmochimica Acta 70, 1128–1147.
Guidry, M.W., Mackenzie, F.T., 2003. Experimental study of igneous and sedimentary apatite dissolution: control of pH, distance from equilibrium, and temperature on dissolution rates. Geochimica Cosmochimica Acta 67, 2949–2963.
Haceb, M.A., 2006. Étude d'un réservoir dans le socle, approche pétrophysique en laboratoire et in situ (en forage): Exemple du site Ringelbach (Hautes-Vosges). Mémoire de Master M2 "Réservoirs Géologiques". LGHF/LT, UM2, Montpellier 29/09/2009, 54 pp.
Helgeson, H.C., Brown, T.H., Nigrini, A., Jones, T.A., 1970. Calculation of mass transfer in geochemical processes involving aqueous solutions. Geochimica Cosmochimica Acta 34, 569–592.
Helgeson, H.C., Murphy, W.M., Aagaard, P., 1984. Thermodynamic and kinetic constraints on reaction rates among minerals and aqueous solutions. II. Rate constants, effective surface area, and the hydrolysis of feldspar. Geochimica Cosmochimica Acta 48, 2405–2432.
Kim, K., 2002. Plagioclase weathering in the groundwater system of a sandy, silicate aquifer. Hydrol. Process. 16 (9), 1793–1806.
Köhler, S.J., Dufaud, F., Oelkers, E.H., 2003. An experimental study of illite dissolution kinetics as a function of ph from 1.4 to 12.4 and temperature from 5 to 50°C. Geochimica Cosmochimica Acta 67, 3583–3594.
Lods, G., Gouze, P., Pézard, P., Ambroise, B., Ertlen, D., Schaffhauser, T., 2011. Site du Ringelbach à Soultzeren, Haut-Rhin, France - Campagne du 11 au 14 octobre 2010-Sondage F-HEI: Single-hole flowmeter test and interpretation. Rapport GSM/TMP-LHyGeS. GSM, Montpellier 8 pp.
Lucas, Y., Schmitt, A.D., Chabaux, F., Clément, A., Fritz, B., Elsass, P., Durand, S., 2010. Geochemical tracing and hydrogeochemical modelling of water/rock interactions during salinization of alluvial groundwater (Upper Rhine Valley, France). Appl. Geochem. 25, 1644–1663.
Madé, B., 1991. Modélisation thermodynamique et cinétique des réactions géochimiques dans les interactions eau-roche. PhD. University of Strasbourg 308pp.
Madé, B., Clément, A., Fritz, B., 1994. Modeling mineral/solution interactions: the thermodynamic and kinetic code KINDISP. Comput. Geosciences 20, 1347–1363.
Maher, K., Steefel, C.I., DePaolo, D.J., Viani, B.E., 2006. The mineral dissolution rate conundrum : insights from reactive transport modeling of U isotopes using U isotopes and pore fluid chemistry in marine sediments. Geochimica Cosmochica Acta 70, 337–363.
Maher, K., Steefel, C.I., White, A.F., Stonestrom, D.A., 2009. The role of reaction affinity and secondary minerals in regulating chemical weathering rates at the Santa Cruz Soil Chronosequence, California. Geochimica Cosmochimica Acta 73, 2804–2831.
Maréchal, J.-C., Wyns, R., Lachassagne, P., Subrahmanyam, K., Touchard, F., 2003. Anisotropie verticale de la perméabilité de l'horizon fissuré des aquifères de socle : concordance avec la structure géologique des profils d'altération. Comptes Rendus Geosci. 335, 451–460.
Marty, N.C.M., Fritz, B., Clément, A., Michau, N., 2010. Modelling the long term alteration of the engineered bentonite barrier in an underground radioactive waste repository. Appl. Clay Sci. Adv. Smectitic clay Res. 47, 82–90.
Mercier, J.L. (Ed.), 1982. Structure et Fonctionnement du Milieu Naturel en Moyenne Montagne–Bassins de la Petite Fecht et du Ringelbach (Vosges, France). Recherches Géographiques à Strasbourg 19-20-21, 276 pp.
Mulla, D.J., McBratney, A.B., 2000. Soil Spatial Variability, Handbook of Soil Science. CRC Press LLC, Boca Raton.
Nicolas, A., 1966. Etude pétrochimique des roches vertes et leurs minéraux entre Dora Maira et Grand Paradis (Alpes piémontaises). Phd.. Université de Nantes 295 pp.
Noack, Y., Nahon, D., Michaux, L., Colin, F., Delvigne, J., 1993. Secondary-mineral formation during natural weathering of pyroxene: review and thermodynamic approach. Am. J. Sci. 293 (2), 111–134.
Oliva, P., Dupré, B., Martin, F., Viers, J., 2004. The role of trace minerals in chemical weathering in a high-elevation granitic watershed (Estibère, France): chemical and mineralogical evidence. Geochimica Cosmochimica Acta 68, 2223–2243.
Palandri, J.L., Kharaka, Y.K., 2004. A Compilation of Rate Parameters of Water-mineral Interaction Kinetics for Application to Geochemical Modeling (No. OPEN-FILE-2004-1068). Geological Survey, Menlo Park CA.
Petschick, R., 2000. Macdiff 4.2.2. Available at: http://servermac.geologie.uni-frankfurt.de/Rainer.html.
Pokrovsky, O.S., Golubev, S.V., Schott, J., 2005. Dissolution kinetics of calcite, dolomite and magnesite at 25 °C and 0 to 50 atm pCO2. Chem. Geol. 217, 239–255.
Pryor, R.W., 2011. Multiphysics Modeling Using COMSOL: a First Principles Approach. Jones and Bartlett publishers.
Rozalen, M., Huertas, F.J., Brady, P.V., 2009. Experimental study of the effect of pH and temperature on the kinetics of montmorillonite dissolution. Geochimica Cosmochimica Acta 73, 3752–3766.
Samuel, J., Rouault, R., Besnus, Y., 1985. Analyse multiélémentaire standardisée des matériaux géologiques en spectrométrie d'émission par plasma à couplage inductif -Geological materials standardized multi-analysis with inductively-coupled plasma emission spectrometry. Analusis 13, 312–317.
Schaffhauser, T., 2013. Traçage et modélisation des processus d'altération à l'échelle d'un petit bassin versant, le Ringelbach (Vosges, France). Thèse de Doctorat. Université de Strasbourg 16/12/2013. LHyGeS/EOST, Strasbourg, 343 pp.
Schaffhauser, T., Chabaux, F., Ambroise, B., Lucas, Y., Stille, P., Reuschlé, T., Perrone, T., Fritz, B., 2014. Geochemical and isotopic (U, Sr) tracing of water pathways in the granitic Ringelbach catchment (Vosges Mountains, France). Chem. Geol. 374–375, 117–127. http://dx.doi.org/10.1016/j.chemgeo.2014.02.028.
Tardy, Y., Fritz, B., 1981. An ideal solid solution model for calculating solubility of clay minerals. Clay Miner. 16, 361–373.
Taylor, A., Blum, J.D., 1995. Relation between soil age and silicate weathering rates determined from the chemical evolution of a glacial chronosequence. Geology 23 (11), 979–982.
Velbel, M.A., 1993. Constancy of silicate-mineral weathering-rate ratios between natural and experimental weathering: implications for hydrologic control of differences in absolute rates. Chem. Geol. 105 (1–3), 89–99.
Viville, D., Ambroise, B., Korosec, B., 1986. Variabilité spatiale des propriétés texturales et hydrodynamiques des sols dans le bassin versant du Ringelbach (Vosges, France). Z. für Geomorphol. N.F. (Suppl. Band 60), 21–40.
White, A.F., Brantley, S.L., 2003. The effect of time on the weathering of silicate minerals: why do weathering rates differ in the laboratory and field? Chem. Geol. 202 (3–4), 479–506.
White, A.F., Schulz, M.S., Lowenstern, J.B., Vivit, D.V., Bullen, T.D., 2005. The ubiquitous nature of accessory calcite in granitoid rocks: implications for weathering, solute evolution, and petrogenesis. Geochimica Cosmochimica Acta 69, 1455–1471.
Wyns, R., Baltassat, J.-M., Lachassagne, P., Legchenko, A., Vairon, J., Mathieu, F., 2004. Application of proton magnetic resonance soundings to groundwater reserve mapping in weathered basement rocks (Brittany, France). Bull. Soc. Geol. Fr. 175, 21–34.
Wyns, R., 2012. Étude géologique du cadre structural et des forages du bassin versant du Ringelbach (Soultzeren, Haut-Rhin). Rapport BRGM/RP-56540-FR, 129 pp.
Zhu, C., 2005. In situ feldspar dissolution rates in an aquifer. Geochim. Cosmochim. Acta 69 (6), 1435–1453.